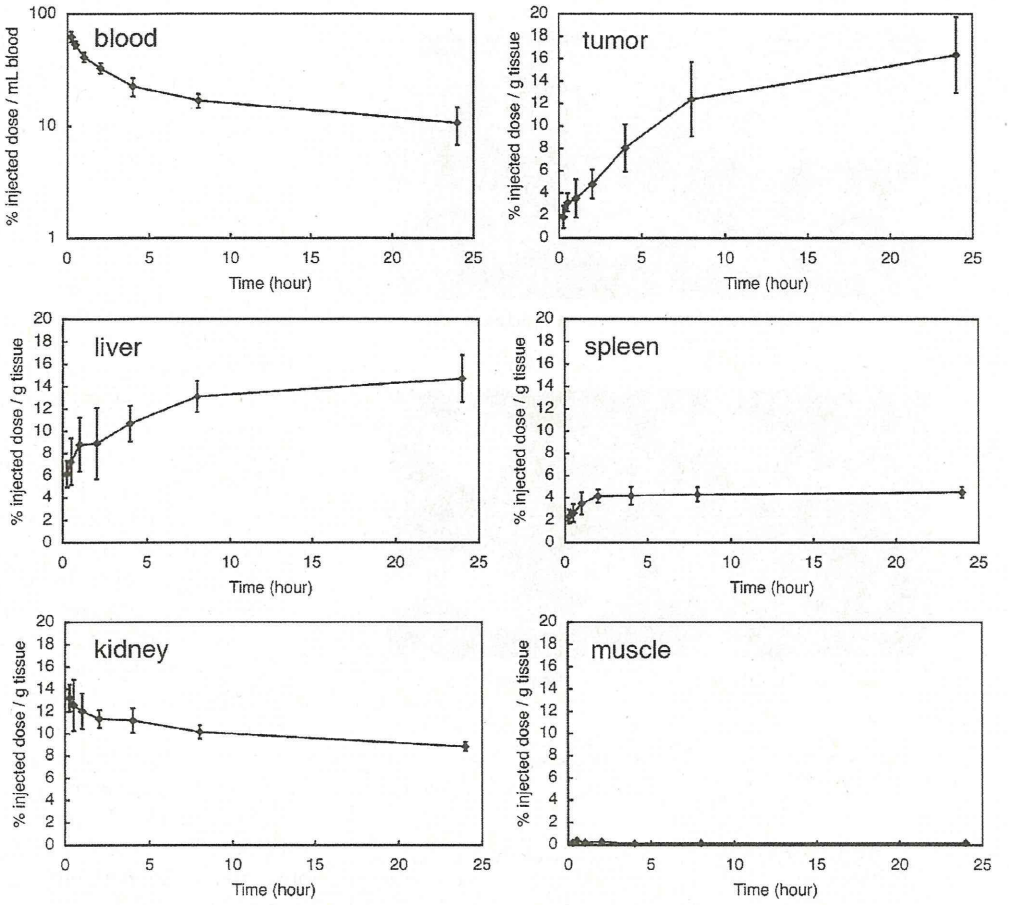

Figure 3. Biodistribution of PEG-AuIONs. The levels of Au in blood, tumor, liver, spleen, kidney, and muscles are shown as percentage of dose at each time after intravenous injection.

(indicated as circled by yellow line in MR images) (Table 1), suggesting that PEG-AuIONs reduced MRI signals more efficiently in the tumor compared with intestine. In contrast, Feridex failed to reduce MRI signals selectively in the tumor even after 4 h (Figure 4b,e and Table 1), presumably due to non-specific accumulation in the RES.

Next, we tested the efficacy of the PEG-AuIONs in an orthotopic pancreatic cancer model, using MiaPaCa-2 cells derived from human pancreatic cancer. The T_2-weighted MR images of the tumor region over time are shown in Figure 4c,d. Noticeable negative enhancement (~25%) was observed as soon as 5 min after administration of PEG-AuIONs, and continued even 4 h after administration (Figure 4c,f and Table 2). It should be noted that PEG-AuIONs exhibited focal MRI signal enhancement in the tumor tissue (indicated by red arrowhead in Figure 4c), presumably due to their heterogeneous intratumoral distribution. The rate of negative enhancement in those regions was calculated to be 47%, which was appreciably higher than that in the intestine (18%) (Table 2). In contrast, Feridex failed in the tumor-selective MRI signal enhancement in this model (Figure 4d,f and Table 2). Furthermore, we tested the effects of the PEG-AuION system compared to Feridex in a model representing metastatic foci in the liver using MiaPaCa-2 cells (Supplementary Figure 1a,b and Supplementary Table 2 in the SI), and the results were consistent with those obtained in the orthotopic model described above. The accumulation of PEG-AuIONs in

Table 1. Percentile rate of negative enhancement in MR signals in the tumor and intestine at 4 h post-injection of PEG-AuION and Feridex into mice bearing a subcutaneous model of murine colon adenocarcinoma (C26) celles.

	Negative enhancement in MRI signals	
	Tumor	**Intestine**
PEG-AuION	60%	25%
Feridex	5%	8%

Macromol. Rapid Commun. **2010**, *31*, 1521–1528

DOI: 10.1002/marc.201000341

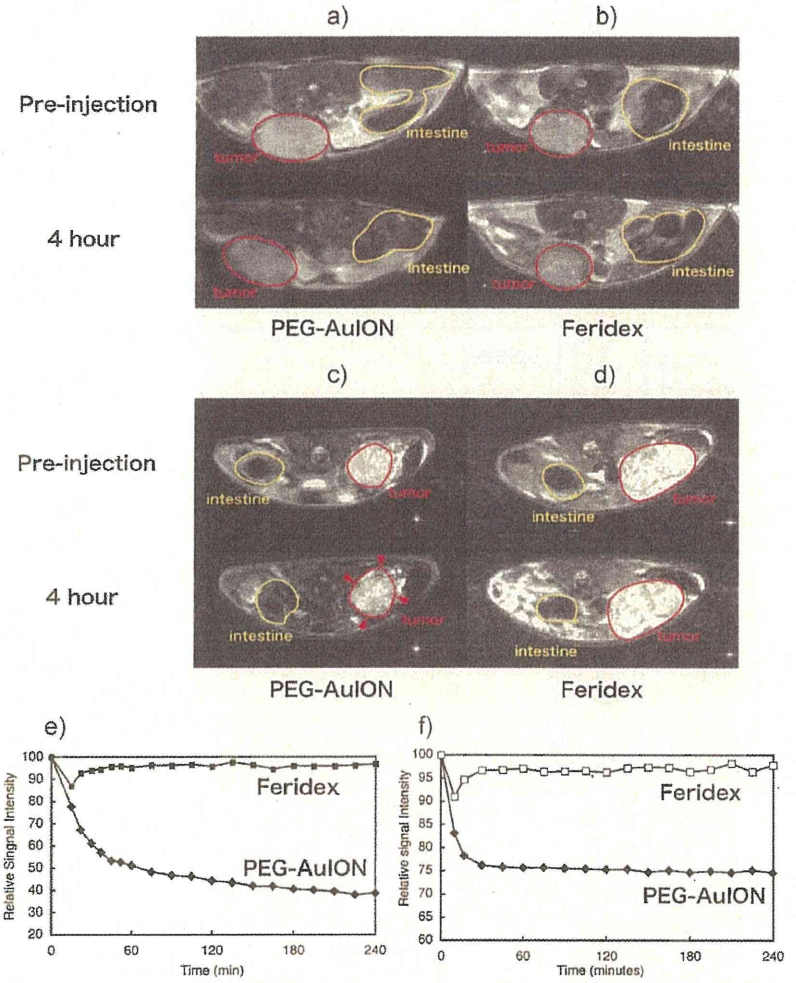

Figure 4. In vivo MR imaging of tumors. a,b) T_2-weighted images of subcutaneous C26 murine carcinoma (tumor sites are circled by red line) at 4 h after intravenous injection of PEG-AuIONs (a) and Feridex (b). c,d) T_2-weighted images of an orthotopic MiaPaCa-2 human pancreatic cancer model (tumor sites are circled by red line) at 4 h after intravenous injection of PEG-AuIONs (c) and Feridex (d). All images were obtained in a magnetic field strength of 4.7 T. Time-dependencies of relative signal intensities at the tumor site in T_2-weighted images after injection of PEG-AuIONs and Feridex in C26 subcutaneous tumor model (e) and in MiaPaCa-2 orthotopic tumor model (f).

metastatic foci was confirmed histologically using silver staining against gold particles (Supplementary Figure 1c in the SI). These results suggest successful MR imaging of malignant tumors is feasible using PEG-AuIONs.

Conclusion

In this study, we have demonstrated that AuIONs of sub-50-nm size and coated with a dense PEG brush can be used as an MRI contrast agent for a variety of tumors, including pancreatic tumors. The relatively small hydrodynamic diameter along with a high PEG density facilitated extended circulation of PEG-AuIONs, which allowed for accumulation into pancreatic cancer models through the EPR effect. These results imply that with proper control of the structural and surface properties of the nanoparticles, it is feasible to develop effective MRI contrast agents for the diagnosis of intractable tumors such as pancreatic cancer, even without attachment of cell-targeting ligands. The presence of an Au shell on the magnetic nanoparticle not only offers the possibility for surface modification with various biomolecules for biomarker-targeted imaging, but also offers another detection modality through various techniques such as X-ray tomography[34–35] (CT) and surface-enhanced Raman scattering (SERS).[36] The ultimate goal of nanoparticle materials for medical research is to develop high-performance systems for both detection and treatment of biological events such as cancer metastasis and real-time visualization of biological events at the cellular and molecular level,

Table 2. Percentile rate of negative enhancement in MR signals in the tumor and intestine at 4 h post-injection of PEG-AuION and Feridex into mice bearing an orthotopic model of human pancreatic adenocarcinoma (MiaPaCa-2) cells.

	Negative enhancement in MRI signals		
	Tumor (whole)	Tumor (arrow head[a)])	Intestine
PEG-AuION	25%	47%	18%
Feridex	3%	–	6%

[a)]The rate of negative enhancement of MRI signals in the regions indicated by red arrowhead in Figure 4c was calculated.

leading to better prognosis in patients bearing tumor. The results of this study represent a significant improvement in nanoparticle-based tumor detection, which may prove useful for clinical applications and also in the design of more advanced systems.

Acknowledgements: The authors thank Dr. *James R. Christie II*, The University of Tokyo, for editing the English of the manuscript. This research was supported by the *Japan Society for the Promotion of Science (JSPS)* through its "Funding Program for World-Leading Innovative R&D on Science and Technology (FIRST Program)". We are grateful to Dr. *S. Fukuda*, The University of Tokyo Hospital, for his valuable support in the TEM measurement. T. K. S. acknowledges a fellowship from the *Japan Society for the Promotion of Science (JSPS)*.

Received: June 8, 2010; Revised: June 30, 2010; DOI: 10.1002/marc.201000341

Keywords: gold coatings; iron oxide; magnetic resonance imaging; nanoparticles; poly(ethylene glycol)

[1] A. Jemal, R. Siegel, E. Ward, Y. P. Hao, J. Q. Xu, M. J. Thun, *CA-A Cancer Journal For Clinicians* **2009**, *59*, 225.
[2] M. J. MacKenzie, *Lancet Oncology* **2004**, *5*, 541.
[3] R. Weissleder, A. Moore, U. Mahmood, R. Bhorade, H. Benveniste, E. A. Chiocca, J. P. Basilion, *Nat. Med.* **2000**, *6*, 351.
[4] H. B. Na, I. C. Song, T. Hyeon, *Adv. Mater.* **2009**, *21*, 1.
[5] Y. W. Jun, J. H. Lee, J. Cheon, *Angew. Chem., Int. Ed.* **2008**, *47*, 5122.
[6] S. Laurent, D. Forge, M. Port, A. Roch, C. Robic, L. V. Elst, R. N. Muller, *Chem. Rev.* **2008**, *108*, 2064.
[7] Y. J. Wang, S. M. Hussain, G. P. Krestin, *Eur. Radiol.* **2001**, *11*, 2319.
[8] Y. Matsumura, H. Maeda, *Cancer Res.* **1986**, *46*, 6387.
[9] H. Maeda, J. Fang, T. Inutsuka, Y. Kitamoto, *Int. Immunopharmacol.* **2003**, *3*, 319.
[10] D. M. McDonald, P. Baluk, *Cancer Res.* **2002**, *62*, 5381.
[11] J. M. Harris, R. B. Chess, *Nat. Rev Drug Discov.* **2003**, *2*, 214.
[12] K. Kataoka, A. Harada, Y. Nagasaki, *Adv. Drug. Delivery Rev.* **2001**, *47*, 113.
[13] C. Khemtong, C. W. Kessinger, J. M. Ren, E. A. Bey, S. G. Yang, J. S. Guthi, D. A. Boothman, A. D. Sherry, J. M. Gao, *Cancer Res.* **2009**, *69*, 1651.
[14] J. F. Berret, N. F. Schonbeck, F. Gazeau, D. El Kharrat, O. Sandre, A. Vacher, M. Airiau, *J. Am. Chem. Soc.* **2006**, *128*, 1755.
[15] H. Lee, M. K. Yu, S. Park, S. Moon, J. J. Min, Y. Y. Jeong, H.-W. Kang, S. Jon, *J. Am. Chem. Soc.* **2007**, *129*, 12739.
[16] E. K. U. Larsen, T. Nielsen, T. Wittenborn, H. Birkedal, T. Vorup-Jensen, M. H. Jakobsen, L. Østergaard, M. R. Horsman, F. Besenbacher, K. A. Howard, J. Kjems, *ACS Nano*, **2009**, *3*, 1947.
[17] M. Kumagai, Y. Imai, M. T. Nakamura, Y. Yamasaki, M. Sekino, S. Ueno, K. Hanaoka, K. Kikuchi, T. Nagano, E. Kaneko, K. Shimokado, K. Kataoka, *Colloids Surf. B* **2007**, *56*, 174.
[18] M. Kumagai, M. R. Kano, Y. Morishita, M. Ota, Y. Imai, N. Nishiyama, M. Sekino, S. Ueno, K. Miyazono, K. Kazunori, *J. Control. Release* **2009**, *140*, 306.
[19] J. L. Lyon, D. A. Fleming, M. B. Stone, P. Schiffer, M. E. Williams, *Nano Lett.* **2004**, *4*, 719.
[20] L. Y. Wang, J. Luo, Q. Fan, M. Suzuki, I. S. Suzuki, M. H. Engelhard, Y. H. Lin, N. Kim, J. Q. Wang, C. J. Zhong, *J. Phys. Chem. B* **2005**, *109*, 21593.
[21] Z. Xu, Y. Hou, S. Sun, *J. Am. Chem. Soc.* **2007**, *129*, 8698.
[22] D. Kim, J. W. Kim, Y. Y. Jeong, S. Jon, *Bull. Korean Chem. Soc.* **2009**, *30*, 1855.
[23] H. Kojima, Y. Mukai, M. Yoshikawa, K. Kamei, T. Yoshikawa, M. Morita, T. Inubushi, T. A. Yamamoto, Y. Yoshioka, N. Okada, S. Seino, S. Nakagawa, *Bioconjugate Chem.* **2010**, *21*, 1026.
[24] S.-J. Cho, B. R. Jarrett, A. Y. Louie, S. M. Kauzlarich, *Nanotechnology* **2006**, *17*, 640.
[25] T. A. Larson, J. Bankson, J. Aaron, K. Sokolov, *Nanotechnology* **2007**, *18*, 325101.
[26] J. W. Cheon, N. J. Kang, S. M. Lee, J. H. Lee, J. H. Yoon, S. J. Oh, *J. Am. Chem. Soc.* **2004**, *126*, 1950.
[27] K. Uchida, H. Otsuka, M. Kaneko, K. Kataoka, Y. Nagasaki, *Anal. Chem.* **2005**, *77*, 1075.
[28] S. Takae, Y. Akiyama, H. Otsuka, T. Nakamura, Y. Nagasaki, K. Kataoka, *Biomacromolecules* **2005**, *6*, 818.
[29] W. P. Wuelfing, S. M. Gross, D. T. Miles, R. W. Murray, *J. Am. Chem. Soc.* **1998**, *120*, 12696.
[30] K. Ohno, T. Morinaga, S. Takeno, Y. Tsujii, T. Fukuda, *Macromolecules* **2007**, *40*, 9143.
[31] S. Kawaguchi, G. Imai, J. Suzuki, A. Miyahara, T. Kitano, K. Ito, *Polymer* **1997**, *38*, 2885.
[32] A. K. Kenworthy, K. Hristova, D. Needham, T. J. McIntosh, *Biophys. J.* **1995**, *68*, 1921.
[33] H. Cabral, N. Nishiyama, K. Kataoka, *J. Controlled Release* **2007**, *121*, 146.
[34] Q. Y. Cai, S. H. Kim, K. S. Choi, S. Y. Kim, S. J. Byun, K. W. Kim, S. H. Park, S. K. Juhng, K. H. Yoon, *Investigative Radiology* **2007**, *42*, 797.
[35] D. Kim, S. Park, J. H. Lee, Y. Y. Jeong, S. Jon, *J. Am. Chem. Soc.* **2007**, *129*, 7661.
[36] X. Qian, X. H. Peng, D. O. Ansari, Q. Yin-Goen, G. Z. Chen, D. M. Shin, L. Yang, A. N. Young, M. D. Wang, S. M. Nie, *Nat. Biotechnol.* **2008**, *26*, 83.

DOI: 10.1002/marc.201000341

Cancer Research

Visible Drug Delivery by Supramolecular Nanocarriers Directing to Single-Platformed Diagnosis and Therapy of Pancreatic Tumor Model

Sachiko Kaida[1,3,7], Horacio Cabral[1,3], Michiaki Kumagai[1], Akihiro Kishimura[2], Yasuko Terada[4], Masaki Sekino[5], Ichio Aoki[6], Nobuhiro Nishiyama[1,3], Toru Tani[7], and Kazunori Kataoka[1,2,3]

Abstract

Nanoparticle therapeutics are promising platforms for cancer therapy. However, it remains a formidable challenge to assess their distribution and clinical efficacy for therapeutic applications. Here, by using multifunctional polymeric micellar nanocarriers incorporating clinically approved gadolinium (Gd)–based magnetic resonance imaging contrast agents and platinum (Pt) anticancer drugs through reversible metal chelation of Pt, simultaneous imaging and therapy of an orthotopic animal model of intractable human pancreatic tumor was successfully performed without any serious toxicity. The strong tumor contrast enhancement achieved by the micelles correlated with the 24 times increase of r_1 of the Gd chelates, the highest for the formulations using clinically approved Gd chelates reported to date. From the microsynchrotron radiation X-ray fluorescence spectrometry scanning of the lesions, we confirmed that both the Gd chelates and Pt drugs delivered by the micelles selectively colocalized in the tumor interior. Our study provides new insights for the design of theranostic micelles with high contrast enhancement and site-specific clinical potential. *Cancer Res; 70(18); 7031–41. ©2010 AACR.*

Introduction

Recently, there has been explosive development of chemotherapeutic agents for cancer, but the efficacies of anticancer drugs are still insufficient particularly for the treatment of intractable tumors, including pancreatic cancer. Although the latest advances in molecular targeting agents have shown specific efficiency, the survival time of patients is often extended only slightly, even when these agents are used in combination with other anticancer drugs. Moreover, the use of such drugs typically results in various characteristic side effects, such as interstitial pneumonia for gefitinib (1), cardiotoxicity for trastuzumab (2, 3), and thrombosis for bevacizumab (4). Alternatives to developing these compounds and antibodies selective for cancer cells, with the aim of modulating drug distribution in the body to accomplish selective drug accumulation in the tumor site, are thus needed, and for this purpose, nanometric-scale vehicles or nanocarriers directing therapeutics to the tumor site are a key platform.

In the last decade, several kinds of nanoparticle therapeutics platforms, including liposomes, nanoparticles, and polymeric micelles, have been developed to selectively deliver drugs to tumor sites (5–12). These approaches have been used to improve the therapeutic efficacy and to reduce the side effects of drugs incorporated in delivery carriers (13, 14), and nanoparticle therapeutics such as Doxil (15) or Abraxane (16) are already in clinical use. The tumor targeting of these nanoparticle therapeutics is based on the enhanced permeability and retention (EPR) effect (in other words, the increased accumulation of high–molecular weight compounds, such as nanoparticles, in tumor tissue due to the high permeability of tumor blood vessels and the retention of these compounds because of the impaired lymphatic drainage at the cancer site; ref. 17). In the late 1980s, we developed one of the auspicious nanoparticle therapeutics, polymeric micelles, a self-assembly of amphiphilic block copolymers consisting of hydrophobic segments forming the drug-loaded core and water-soluble segments forming the biocompatible shell (11, 12). The main advantages of this system are the possibility of incorporating a variety of drugs, including hydrophobic substances, metal complexes, and charged macromolecules such as nucleic acids, as well as controlling their release properties by engineering and modifying the micelle-forming block copolymers. Moreover, polymeric micelles can be designed to be responsive to environmental changes and capable of target

Authors' Affiliations: [1]Center for Disease Biology and Integrative Medicine, Graduate School of Medicine, [2]Department of Materials Engineering, Graduate School of Engineering, and [3]Center for NanoBio Integration, The University of Tokyo, Tokyo, Japan; [4]Japan Synchrotron Radiation Research Institute, SPring-8, Hyogo, Japan; [5]Department of Advanced Energy, Graduate School of Frontier Sciences, The University of Tokyo, Chiba, Japan; [6]Molecular Imaging Center, National Institute of Radiological Sciences, Chiba, Japan; and [7]Department of Surgery, Shiga University of Medical Science, Shiga, Japan

Note: Supplementary data for this article are available at Cancer Research Online (http://cancerres.aacrjournals.org/).

Corresponding Author: Kazunori Kataoka, Department of Materials Engineering, Graduate School of Engineering, The University of Tokyo, 7-3-1 Hongo, Bunkyo-ku, Tokyo 113-8656, Japan. Phone: 81-3-5841-7138; Fax: 81-3-5841-7139; E-mail: kataoka@bmw.t.u-tokyo.ac.jp.

doi: 10.1158/0008-5472.CAN-10-0303

recognition. Our micelle formulations incorporating Adriamycin, paclitaxel, SN-38, cisplatin, and DACHPt (activated oxaliplatin; NK911, NK105, NK012, NC6004, and NC4016, respectively) are being examined in clinical studies, and four of these formulations have advanced to phase II studies (18–21). These clinical studies have revealed that polymeric micelles showed reduced side effects and high effectiveness against various intractable tumors, including triple-negative breast cancers that do not express the genes for estrogen receptor, progesterone receptor, and Her2/neu (22). Consequently, polymeric micelles have been considered one of the most promising drug delivery systems (DDS) in the field of cancer chemotherapy.

Although a crucial breakthrough in cancer treatment has been achieved using several micelles, the methods for estimating the distribution and effectiveness of the micelles are ineffective and inadequate. The precise monitoring of their distribution and early feedback on treatment efficacy would allow clinicians to anticipate the therapeutic process in each cancer patient and customize medicine for cancer therapy. Thus, it is imperative to directly assess the biodistribution of the micelles and their cargo as well as the magnitude of their accumulation at the cancer site. Consequently, the development of micelles with both imaging and therapeutic functions [theranostic (23) micelles] will permit visualization of the distribution of the micelles inside the body and tumor in a real-time manner, allowing optimization of the treatment protocol according to the unique characteristics of the malignancies in individual patients (24–26).

We developed theranostic core-shell polymeric micelles based on the self-assembly of block copolymers with both a magnetic resonance imaging (MRI) function and cancer therapeutic capacity. The micelles incorporate gadolinium–diethylenetriaminepentaacetic acid (Gd-DTPA), a widely used T_1-weighted MRI (T1W) contrast agent (27), and (1,2-diaminocyclohexane)platinum(II) (DACHPt), the parent complex of the potent anticancer drug oxaliplatin, in their core by reversible complexation between DACHPt, Gd-DTPA, and poly(ethylene glycol)-*b*-poly(glutamic acid) [PEG-*b*-P(Glu); Fig. 1]. Accordingly, both the DACHPt and Gd-DTPA complexes, which can be excreted from the kidney, thus avoiding toxicity from long-term accumulation inside the body, are released from the micelles in a sustained manner under physiologic conditions. Moreover, the longitudinal relaxivity (r_1) of the micelles (i.e., their ability as an MRI contrast agent) increased ~24 times compared with that of free

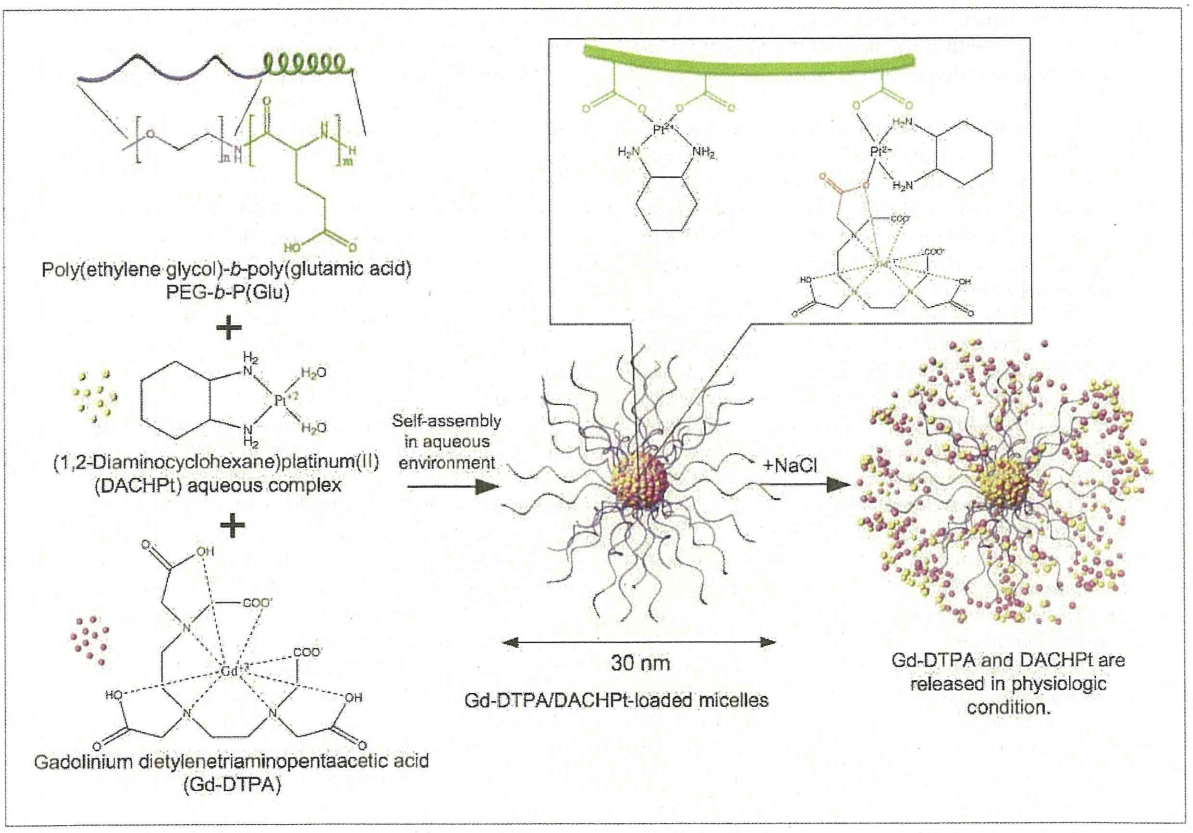

Figure 1. Schematic diagram of proposed self-assembly of Gd-DTPA/DACHPt–loaded micelles and release of Pt and Gd complexes from the micelles in chloride-containing medium.

Gd-DTPA, enabling, jointly with the enhanced tumor accumulation provided by the EPR effect, the improved detection of solid tumors. We also showed that the micelles have continuous and strong anticancer effect, and enhance the MRI contrast of the tumor region in an orthotopic human pancreatic cancer xenograft model much more intensely than Gd-DTPA alone, although the diagnosis and treatment of pancreatic cancer has been considered to be the most difficult among digestive cancers. Thus, the Gd-DTPA/DACHPt–loaded micelles are expected not only to improve the effectiveness and safety of the incorporated drugs but also to assist in the real-time monitoring of the drug distribution and tumor accumulation, suggesting the great potential of visible DDSs.

Materials and Methods

Cancer cell lines and animals

Murine colon adenocarcinoma 26 (C-26) cells were kindly supplied by the National Cancer Center. The BxPC3 human pancreatic adenocarcinoma cell line was obtained from the American Type Culture Collection. C-26 and BxPC3 cells were maintained in RPMI 1640 (Sigma-Aldrich, Inc.) containing 10% fetal bovine serum in a humidified atmosphere containing 5% CO_2 at 37°C. CDF_1 mice and BALB/c nude mice (female; 18–20 g body weight; 6 weeks old) were purchased from Charles River Japan. All animal experiments were carried out in accordance with the policies of the Animal Ethics Committee of the University of Tokyo.

Preparation of Gd-DTPA/DACHPt–loaded micelles

PEG-*b*-P(Glu) [Mw_{PEG} = 12,000 Da; polymerization degree of P(Glu) = 20] block copolymer was synthesized according to the previously described method (28). Briefly, the *N*-carboxy anhydride of γ-benzyl L-glutamate (Sigma Chemical) was synthesized by the Fuchs-Farthing method using triphosgene. Then, *N*-carboxy anhydride of γ-benzyl L-glutamate was polymerized in DMF initiated by the primary amino group of CH_3O-PEG-NH_2 (Nippon Oil and Fats) to obtain PEG-*b*-poly (γ-benzyl-L-glutamate) (PEG-*b*-PBLG). The polymerization degree was verified by comparing the proton ratios of methylene units in PEG (-OCH_2CH_2-: δ = 3.7 ppm) and phenyl groups of PBLG (-$CH_2C_6H_5$: δ = 7.3 ppm) in ^{1}H nuclear magnetic resonance (NMR) measurement (solvent: DMSO-d_6; JEOL EX270, JEOL, Inc.). PEG-*b*-PBLG was deprotected by mixing with 0.5 N NaOH at room temperature to obtain PEG-*b*-P(Glu). Complete deprotection was confirmed by ^{1}H-NMR measurement (solvent: D2O; temperature: 25°C).

Gd-DTPA (Aldrich Chemical) was converted to sodium salt by adjusting the pH to 7 with NaOH, and it was lyophilized. A 5 mmol/L solution of bis(nitrato) (*trans-l*-1,2-diaminocyclohexane)platinum(II) [DACHPt(NO_3)$_2$; W.C. Heraeus GmbH & Co. KG] in water was mixed with the sodium salt of Gd-DTPA (5 mmol/L), and the solution was maintained for 24 hours at 37°C. Then, PEG-*b*-P(Glu) ([Glu] = 5 mmol/L) was added to this solution ([DACHPt]/[Glu] = 1.0) and reacted for 120 hours at 37°C to prepare Gd-DTPA/DACHPt–loaded micelles. The micelles were purified by dialysis against distilled water [molecular weight cutoff size (MWCO): 2,000; Spectra/Por-6, Spectrum Laboratories] and by ultrafiltration (MWCO: 30,000). The size distribution of the Gd-DTPA/DACHPt–loaded micelles was evaluated by a dynamic light scattering (DLS) measurement at 25°C using a Zetasizer Nano ZS90 (Malvern Instruments). The Pt and Gd contents of the micelles were determined by inductively coupled plasma–mass spectrometry (ICP-MS; 4500 ICP-MS, Hewlett Packard).

Fourier transform IR spectra of Gd-DTPA/DACHPt aqueous complex

Fourier transform IR (FT-IR) spectra were obtained using a FT-IR spectrophotometer (FT/IR 615, JASCO Corp.) with a resolution of 4 cm^{-1}. To characterize the interaction between Gd-DTPA and DACHPt, freeze-dried Gd-DTPA/DACHPt complex at 1:1, 1:5, and 1:10 mixing ratios was milled with KBr and then pressed into a disc for analysis.

Arsenazo III colorimetric assay

The absence of Gd^{3+} in the Gd-DTPA/DACHPt mixture was confirmed by using the arsenazo III method (29). Briefly, Gd-DTPA and DACHPt were mixed at 1:1 molar ratio (0.2 mmol/L) in water. Then, 0.5 mL of this solution was mixed with 0.5 mL of arsenazo III (0.2 mmol/L; Sigma-Aldrich). The absorbance spectra were measured with a spectrometer (V-570 UV/VIS/NIR Spectrophotometer, JASCO). A calibration curve was obtained by measuring the absorbance at 660 nm of a series of standard solutions of the arsenazo III/Gd^{3+} complex prepared by mixing solutions of $GdCl_3$ (Sigma-Aldrich) and arsenazo III in water. The pH of the solutions was maintained at 6.5.

Release rate of DACHPt and Gd-DTPA from the Gd-DTPA/DACHPt–loaded micelles

The release of DACHPt and Gd-DTPA complexes from the micelles was studied by the dialysis method. One milliliter of Gd-DTPA/DACHPt–loaded micelles solution was introduced in a dialysis bag (MWCO: 6,000) and incubated in 99 mL micelles in physiologic conditions (i.e., 10 mmol/L PBS plus 150 mmol/L NaCl at 37°C). The solution outside the dialysis bag was sampled at defined periods. The concentration of Pt and Gd was measured by ICP-MS. The UV-Vis spectra of Gd-DTPA, $GdCl_3$, and the solution outside the dialysis bag were recorded from 270 nm to 280 nm with a UV-Vis spectrometer (V-570 UV/VIS/NIR Spectrophotometer).

Kinetic stability of Gd-DTPA/DACHPt–loaded micelles

The stability of the Gd-DTPA/DACHPt–loaded micelles in physiologic conditions was determined by DLS and static light scattering using a Zetasizer Nano ZS90. The changes in the light scattering intensity were measured at defined time periods. In this analysis, a decrease in the light scattering intensity was associated with a decrease in the apparent molecular weight of the micelles and drug density inside the micelle core as well as in the micelle concentration. The size distribution of the Gd-DTPA/DACHPt–loaded micelles was simultaneously monitored.

Characterization of the r_1 relaxivities

The MR contrast effect of the magnetic nanoparticles was examined by measuring their proton longitudinal relaxivities, r_1, of which the definition is the slope of the concentration dependence given as $1/T_1 = 1/T_{10} + r_1[\mathrm{Gd}]$, where T_1 is the longitudinal relaxation time, $1/T_1$ is the longitudinal relaxation rate contrast in the presence of a paramagnetic species, and $1/T_{10}$ is the longitudinal relaxation rate contrast in the absence of a paramagnetic species. The T_1 of Gd-DTPA/DACHPt–loaded micelles, Gd-DTPA, or Gd-DTPA/DACHPt solution at 0.1, 0.2, 0.3, 0.4, and 0.5 mmol/L was measured at 37°C in water with a 0.59-T ^{1}H-NMR analyzer (JNM-MU25A, JEOL) with a standard inversion-recovery pulse sequence.

Cancer models

CDF_1 mice (female, 6 weeks old) were inoculated s.c. with C-26 cells (1×10^6/mL) and used for biodistribution study, antitumor activity assay, and MRI. BALB/c nude mice (female, 6 weeks old) were inoculated in the pancreas with BxPC3 cells for biodistribution study, antitumor activity assay, and MRI. For the latter model, the mice were anesthetized by isoflurane inhalation, and the pancreas was exposed and injected subserosally with 0.1 mL of BxPC3 cells (5×10^6/mL).

Biodistribution

Biodistribution studies were carried out on C-26 tumor–bearing mice at 10 days after implantation when the mean tumor volume was ~100 mm^3. Oxaliplatin, Gd-DTPA, or Gd-DTPA/DACHPt–loaded micelles were i.v. injected to mice at a dose of 100 μg per mouse on a Pt basis or 100 μg per mouse on a Gd basis. The mice were sacrificed after defined time periods (1, 4, 8, and 24 hours). Tumors, livers, kidneys, and spleens were excised. Blood was collected from the inferior vena cava, heparinized, and centrifuged to obtain the plasma. The samples were dissolved in HNO_3 and evaporated to dryness. The Pt and Gd concentrations were then measured by ICP-MS after the samples were redissolved in 5 N HCl.

In vivo MRI of Gd-DTPA/DACHPt–loaded micelles

MR images were obtained using a 4.7-T UNITY INOVA imaging spectrometer (Varian, Inc.) equipped with a birdcage-type RF coil, 66 mm in diameter. For the T1W of the mice, the following parameters were adopted: spin-echo method, repetition time (TR) = 500 ms, echo time (TE) = 15 ms, field of view (FOV) = 32 × 32 mm^2, matrix size = 256 × 256, and slice thickness = 2 mm. MR images were obtained from C-26 tumor– and BxPC3 tumor–bearing mice when the mean tumor volume was 100 and 400 mm^3, respectively. For all of the mice, transaxial T1W images were taken before injecting Gd-DTPA/DACHPt–loaded micelles as a control. The mice were anesthetized with 1.2% isoflurane during the MRI experiments. The mice were injected i.v. with 5 μmol/kg of Gd-DTPA alone or Gd-DTPA/DACHPt–loaded micelles. The transaxial T1W images were taken with a phantom containing water as a reference signal every 10 minutes for 4 hours. The images were analyzed using Mathematica (Wolfram Research, Inc.) and Excel (Microsoft, Inc.). For each time point, the same level of slices that included the center of the tumors was chosen and segmented by drawing a square that included the tumor area. The pixel intensities in the tissues were compared with the precontrast images and the phantom.

Assessment of therapeutic effect by MRI

MR images were obtained using a 7.0-T MRI scanner (magnet: Kobelco and Jastec; console: Bruker Biospin) with a birdcage-type RF coil, 35 mm in diameter (Rapid Biomedical). The experiment was carried out on BxPC3 tumor–bearing mice at 10 days after implantation when the average size of the tumor was ~60 mm^3. Mice (n = 2) were initially anesthetized with 3.0% isoflurane, orally intubated, and then ventilated with 2.0% isoflurane (Abbott Japan) and 1:2 O_2/room air gas mixture using a rodent ventilator (MRI-1, CWE, Inc.). During MRI scanning, rectal temperature was continuously monitored and maintained at 37.0 ± 0.5°C using a heating pad throughout all scans. T1W MRIs were obtained before and 2 hours after administration of the Gd-DTPA/DACHPt–loaded micelles. The Gd-DTPA/DACHPt–loaded micelles were injected i.v. at 8 mg/kg on a Pt base and 3 mg/kg on a Gd-DTPA base. The control mice were injected i.v. with 30 mg/kg of Gd-DTPA, and they were imaged before and 30 minutes after the injection. The drugs were injected on days 0, 4, 8, 11, and 18. T1W multislice two-dimensional spin echo MRI with fat suppression preparation was obtained with the following parameters: TR = 600 ms (respiratory gating of 100 rpm), TE = 9.5 ms, FOV = 32 × 32 mm^2, matrix size = 256 × 256, slice thickness = 1 mm, and average = 4. Slice orientation of the T1W was transaxial (18 slices, nongap) and horizontal (14 slice, nongap).

Image reconstruction and analysis were performed using ParaVision (version 4.0; Bruker Biospin) and ImageJ (version 1.43; NIH). Regions of interest were identified using a mouse atlas of anatomy, and the volume of the tumors was estimated by the following equation: $V = a \times b^2/2$, where a and b are the major and minor axes of the orthotopic tumors measured from the MR images.

Histology and immunohistochemistry

The excised samples were directly frozen in liquid N_2 for immunohistochemistry or fixed in 4% paraformaldehyde and then paraffin embedded to prepare them for H&E staining. Frozen samples were sectioned at 16-μm thickness in a cryostat, fixed in acetone, and incubated with protein blocking solution (Blocking One Buffer, Nakalai Tesque, Inc.), PECAM-1 (BD Pharmingen), Alexa Fluor 488 secondary antibody (Invitrogen Molecular Probes), and Hoechst (Sigma-Aldrich). The samples were observed by using a Zeiss LSM510 Meta confocal microscope for immunohistochemistry and an Olympus AX80 microscope for H&E staining.

Micro-synchrotron radiation X-ray fluorescence spectrometry analysis

Mice bearing BxPC3 orthotopic tumors were injected i.v. with doses of 3 mg/kg (on a Pt base) of Gd-DTPA/DACHPt–loaded micelles. Four hours after the injection, the mice were

sacrificed and the tumors were excised, frozen in liquid N_2, sliced at 16 μm using a cryostat, and fixed on a polypropylene sheet. Micro-synchrotron radiation X-ray fluorescence spectrometry (μ-SR-XRF) was performed using beamline 37XU (30) at SPring-8, operated at 8 GeV and ~100 mA. The tissue samples were irradiated with incident X-rays with an energy of 14 keV, a beam spot size of 1.3 × 1.3 μm^2, and an intensity of 10^{12} photons/s. The fluorescence X-rays were measured using a Si solid-state detector in air at room temperature. Each sample was mounted on an *x-y* translation stage. The fluorescence X-ray intensity was normalized by the incident X-ray intensity, I_0, to produce a two-dimensional elemental map.

Results

Characterization of Gd-DTPA/DACHPt–loaded micelles

The core-shell micellar nanocarriers with PEG palisade were prepared by preincubating Gd-DTPA and DACHPt at a 1:1 molar ratio for >10 hours in water and mixing this solution with PEG-*b*-P(Glu) (Fig. 1). The incubation of DACHPt with Gd-DTPA may lead to the formation of carboxylato complexes between DACHPt and the carboxylic groups in the DTPA chelator of Gd-DTPA. Accordingly, the FT-IR spectra of the DACHPt, Gd-DTPA, and Gd-DTPA/DACHPt mixtures incubated for 24 hours (Fig. 2A) indicated the appearance of a peak at 1,650 cm^{-1} in the spectra of the Gd-DTPA/DACHPt mixtures assigned to the Pt-COO coordination bond. Moreover, the optimal mixing ratio and incubation time of Gd-DTPA and DACHPt were determined by relaxivity titration. The r_1 of the Gd-DTPA/DACHPt complexes gradually increased up to 4.6 $mmol/L^{-1}s^{-1}$ at a 1:1 ratio from the initial 3.4 $mmol/L^{-1}s^{-1}$ of Gd-DTPA alone (Supplementary Fig. S1A). At DACHPt/Gd-DTPA ratios higher than 1, the r_1 remained constant. In addition, the r_1 of the Gd-DTPA/DACHPt complex gradually increased until 10 hours after mixing. Moreover, the activated state of DACHPt was found to be necessary for binding to Gd-DTPA because the Gd-DTPA/oxaliplatin mixture revealed no increase in the relaxivity (Supplementary Fig. S1B). During the Gd-DTPA/DACHPt complex formation, the stability of the Gd-DTPA complex was evaluated by using the arsenazo III method (29). Consequently, the absence of Gd^{3+}

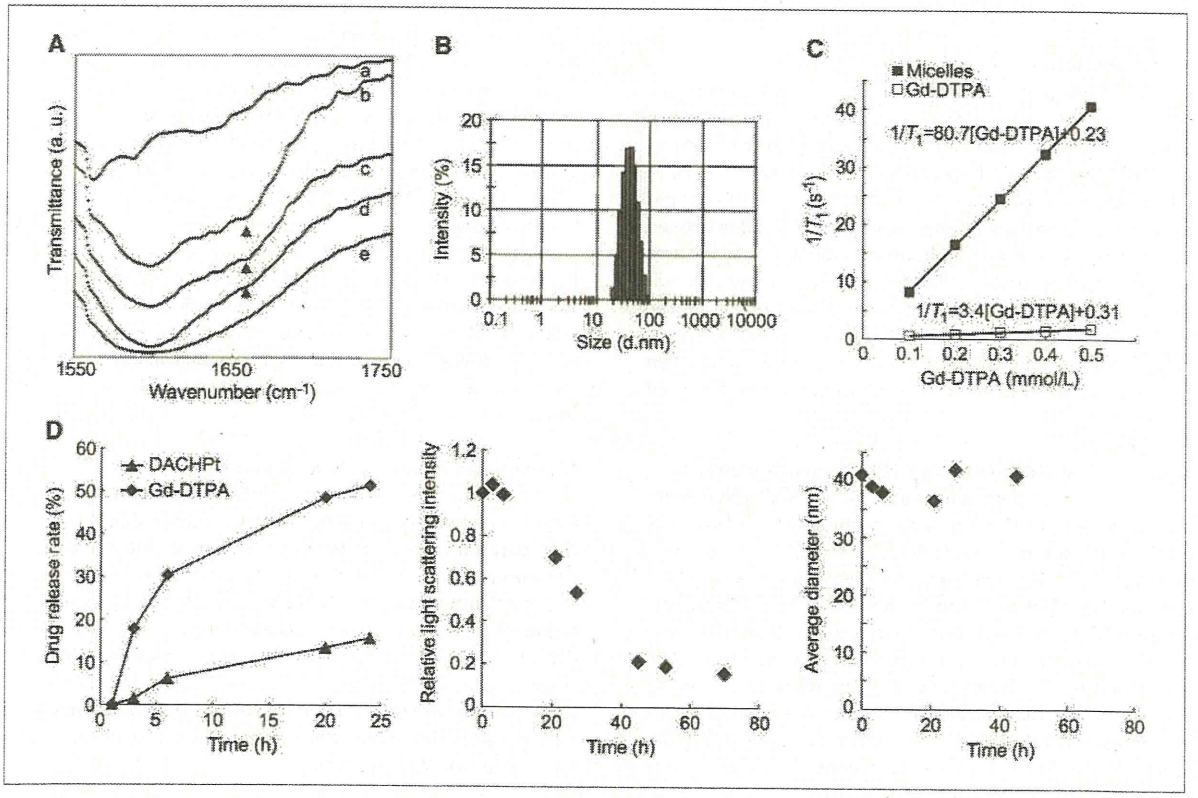

Figure 2. Formation and physicochemical characteristics of Gd-DTPA/DACHPt–loaded micelles. A, FT-IR spectra of DACHPt (a); Gd-DTPA/DACHPt complexes 1:1 (b), 5:1 (c), and 10:1 (d); and Gd-DTPA (e). B, diameter of the micelles determined by DLS. C, longitudinal relaxation ($1/T_1$) of micelles and Gd-DTPA at 37°C. The longitudinal relaxivities (r_1) were calculated from the slope. D, left, release rate of Pt and Gd complexes from Gd-DTPA/DACHPt–loaded micelles in physiologic conditions; middle, relative light scattering intensity of the Gd-DTPA/DACHPt–loaded micelles in physiologic conditions; right, diameter of Gd-DTPA/DACHPt–loaded micelles in physiologic conditions.

in the Gd-DTPA/DACHPt mixture was confirmed (Supplementary Fig. S2).

The obtained micelles were 33 nm in diameter with a narrow size distribution (polydispersity index = 0.067; Fig. 2B). This diameter might be small enough for the micelles to avoid recognition by the reticuloendothelial system, pass through the leaky vasculature of solid tumors by the EPR effect, and attain deep tumor penetration (17). The amounts of DACHPt and Gd-DTPA incorporated in the micelles were found to be 0.42 mg DACHPt/mg polymer and 0.04 mg Gd-DTPA/mg polymer, corresponding to 45% and 5% of the carboxylic groups in PEG-*b*-P(Glu), respectively. Moreover, the r_1 of the micelles increased up to 80.7 $mmol/L^{-1}s^{-1}$, that is, ~24-fold greater than Gd-DTPA alone (Fig. 2C).

The Gd-DTPA/DACHPt–loaded micelles did not release their contents in distilled water (data not shown). However, under physiologic conditions (i.e., 10 mmol/L PBS at 37°C), DACHPt and Gd-DTPA were released in a sustained manner (Fig. 2D, left). Moreover, the release of Gd-DTPA was considerably faster than that of DACHPt, probably due to stronger binding between polymer and DACHPt than between DACHPt and Gd-DTPA. In addition, the safe Gd-DTPA chelates in this system might remain stable because no free Gd^{3+} was detected in the released sample (Supplementary Fig. S3). The gradual drug release from Gd-DTPA/DACHPt–loaded micelles led to a reduction in the light scattering intensity of the micelles (Fig. 2D, middle) due to the decreased density of the micellar cores. Accordingly, the light scattering intensity of the Gd-DTPA/DACHPt–loaded micelles under physiologic conditions decreased to 20% in ~60 hours (Fig. 2D, middle); however, the hydrodynamic diameter of the micelles was maintained at ~30 nm for >48 hours (Fig. 2D, right). The high stability of the micelles and preservation of their hydrodynamic diameter are advantageous in the *in vivo* situation because the structural stability of micelles is highly associated with their prolonged blood circulation (11).

In vivo performance of Gd-DTPA/DACHPt–loaded micelles

The Gd-DTPA/DACHPt–loaded micelles extended the circulation of their cargo in the bloodstream, attaining ~20% of the injected dose of DACHPt after 24 hours and >8% of the injected dose of Gd-DTPA after 4 hours, whereas free oxaliplatin and free Gd-DTPA were rapidly cleared from plasma (Fig. 3A). Moreover, the micelles delivered the drugs to solid tumors due to the increased accumulation and retention at the cancer site because of the EPR effect. Accordingly, the micelles augmented the tumor accumulation 27.7 times for the Pt drug at 24 hours, and >100 times for Gd-DTPA at 4 hours, in subcutaneous murine colon adenocarcinoma 26 (C-26) tumors (Fig. 3B) compared with oxaliplatin and free Gd-DTPA, resulting in high MRI contrast enhancement of the tumor tissue (Fig. 3C). From the ratio of the signal intensities of tumor to muscle, the micelles showed to increase the contrast, whereas the enhancement for Gd-DTPA was almost unchanged. Moreover, the elevated tumor accumulation of Gd-DTPA/DACHPt–loaded micelles may also improve the antitumor activity of the incorporated Pt drug because DACHPt complexes can exert their cytotoxicity after being released from the Gd-DTPA/DACHPt–loaded micelles, as observed in *in vitro* studies (Supplementary Table S1). Accordingly, the micelles showed strong antitumor effect against the C-26 tumor model (Supplementary Fig. S4). Thus, we tested the potential of Gd-DTPA–loaded micelles for monitoring the drug distribution, tumor imaging, and treatment in a pancreatic tumor model close to the clinical situation (i.e., orthotopically inoculated BxPC3 human pancreatic ductal adenocarcinoma tumor).

Direct detection and treatment of pancreatic cancer

The T1W T_1-weighted MR images after i.v. administration of the Gd-DTPA/DACHPt–loaded micelles clearly showed specific contrast enhancement at the tumor area for >4 hours (Fig. 4A and B). In contrast, we did not observe any enhancement in the tumor region after the administration of free Gd-DTPA (Fig. 4A and B), and the signal intensity was higher in the liver, kidney, or spleen than in tumor as suggested from the tumor-to-organ ratios of the MR intensity (Supplementary Table S2). Also, the signals in all organs decreased after 1 hour. The macroscopic observation of the orthotopic tumor-bearing mice that received Gd-DTPA/DACHPt–loaded micelles confirmed the position of every organ and the tumor (Fig. 4D, left and middle), whereas the histologic study of the malignancy revealed the poorly differentiated histology of pancreatic adenocarcinoma, with thick fibrosis and low vascularization (Fig. 4D, right). The amount of Gd-DTPA delivered by the micelles in the orthotopic pancreatic tumor was seven times higher than the accumulation of free Gd-DTPA (Fig. 4C). Accordingly, 3.5% of the total Gd dose from the micelles and 7.2% of the total Pt dose had accumulated within 4 hours of administration.

The antitumor activity of Gd-DTPA/DACHPt–loaded micelles was also evaluated by MRI. Thus, the mice treated with the micelles at 8 mg/kg on a Pt base achieved a significant reduction in the volume of orthotopic BxPC3 tumors (Fig. 5A). Likewise, the weight of the pancreas at day 18 of the micelle-treated animal was much lower than the mice that received only Gd-DTPA (Fig. 5B). Moreover, Gd-DTPA/DACHPt–loaded micelles were shown to enhance the signal intensity at the tumor region (Fig. 5C). Thus, Gd-DTPA/DACHPt–loaded micelle can be used to follow the micelle accumulation in the tumor and the tumor size by MRI, supporting the theranostic concept.

The microdistribution of the drugs at the tumor site was studied using μ-SR-XRF on the pancreatic lesions. Besides the elements traditionally present in animal tissue, such as S, Cl, K, Ca, Fe, Cu, Ni, and Zn, very distinct Pt-L and Gd-L peaks can also be observed in the sum spectrum of the line scan. Thus, the distribution of several atoms (Fe, K, Gd, and Pt) in the tissue sections of the whole pancreas was studied to evaluate the tissue properties and layout of the drugs. The elemental mapping of Fe presents areas with high concentration probably involving the vicinity of blood vessels and the

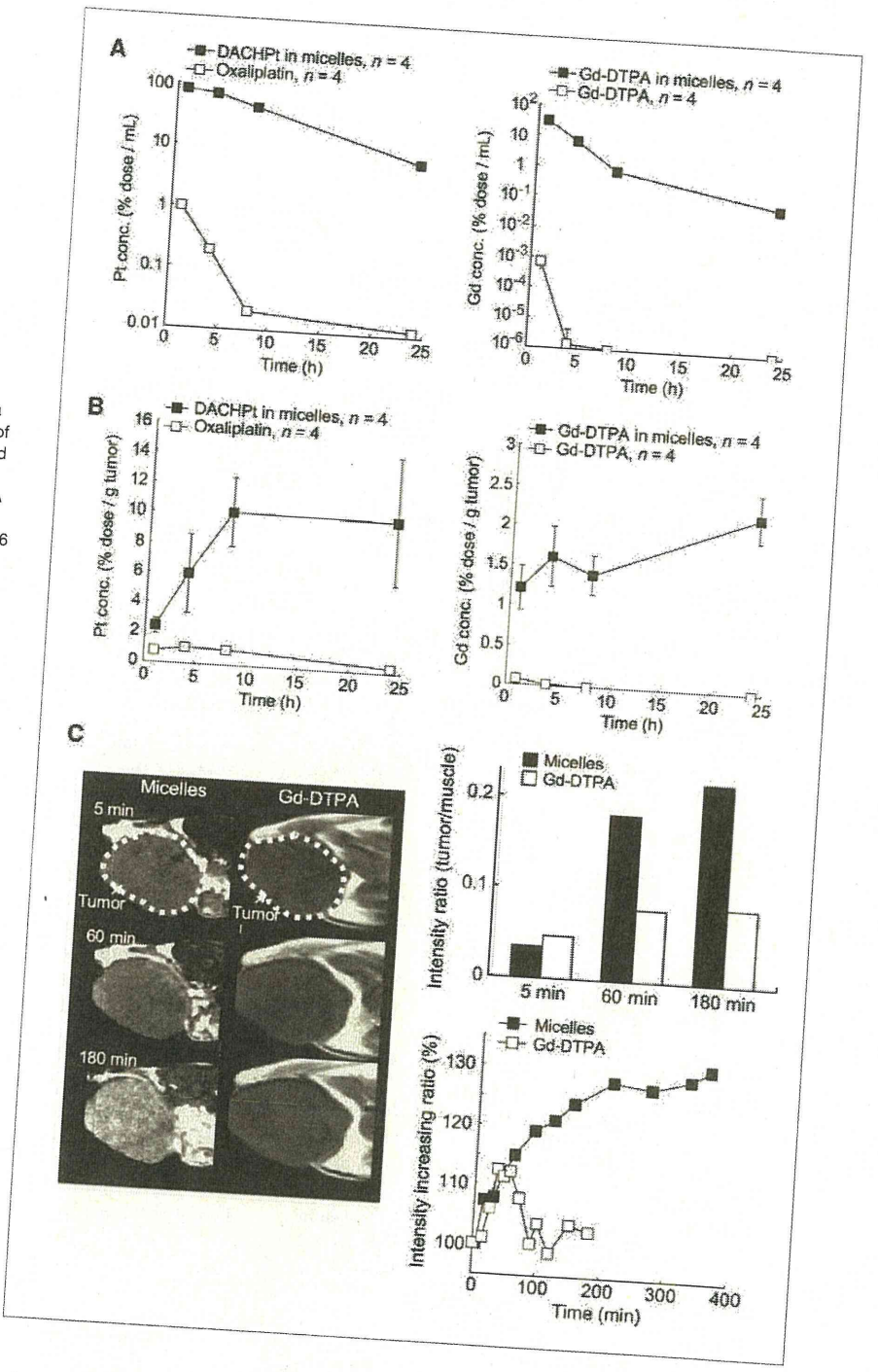

Figure 3. *In vivo* behavior of Gd-DTPA/DACHPt–loaded micelles. A, left, plasma clearance of Pt drugs after i.v. injection of oxaliplatin and Gd-DTPA/DACHPt–loaded micelles; right, plasma clearance of Gd complexes after i.v. injection of Gd-DTPA and Gd-DTPA/DACHPt–loaded micelles. B, left, accumulation of Pt drugs in the C-26 tumor after i.v. injection of oxaliplatin or Gd-DTPA/DACHPt–loaded micelles; right, accumulation of Gd complexes in C-26 tumors after i.v. injection of Gd-DTPA or Gd-DTPA/DACHPt–loaded micelles. C, left, *in vivo* MRI series of T_1-weighted transaxial slices of C-26 subcutaneous tumor after i.v. injection of Gd-DTPA/DACHPt–loaded micelles or Gd-DTPA at 5 μmol/kg Gd-DTPA. Right, top, tumor-to-muscle intensity ratio for the micelles and Gd-DTPA at 5, 60, and 180 min; bottom, relative intensity enhancement in the tumor after i.v. injection of Gd-DTPA/DACHPt–loaded micelles or Gd-DTPA at 5 μmol/kg Gd-DTPA.

distribution of heme proteins. Accordingly, the PECAM-1–positive area from the immunofluorescence microscopy (Fig. 6A) showing the existence of endothelial cells is consistent with this Fe-rich area (Fig. 6B). The K-rich regions possibly correspond to pancreatic cancer cells because K is a cofactor required to obtain maximum activity of the pyruvate kinase, an enzyme involved in glycolytic energy production, which has been observed in carcinoma tissue of the pancreas (31). The Gd as well as the Pt atoms located at those K-rich areas suggest the selective tumor accumulation of Gd-DTPA and DACHPt. Moreover, the colocalization of the Gd-DTPA and DACHPt confirms the high potential of Gd-DTPA/

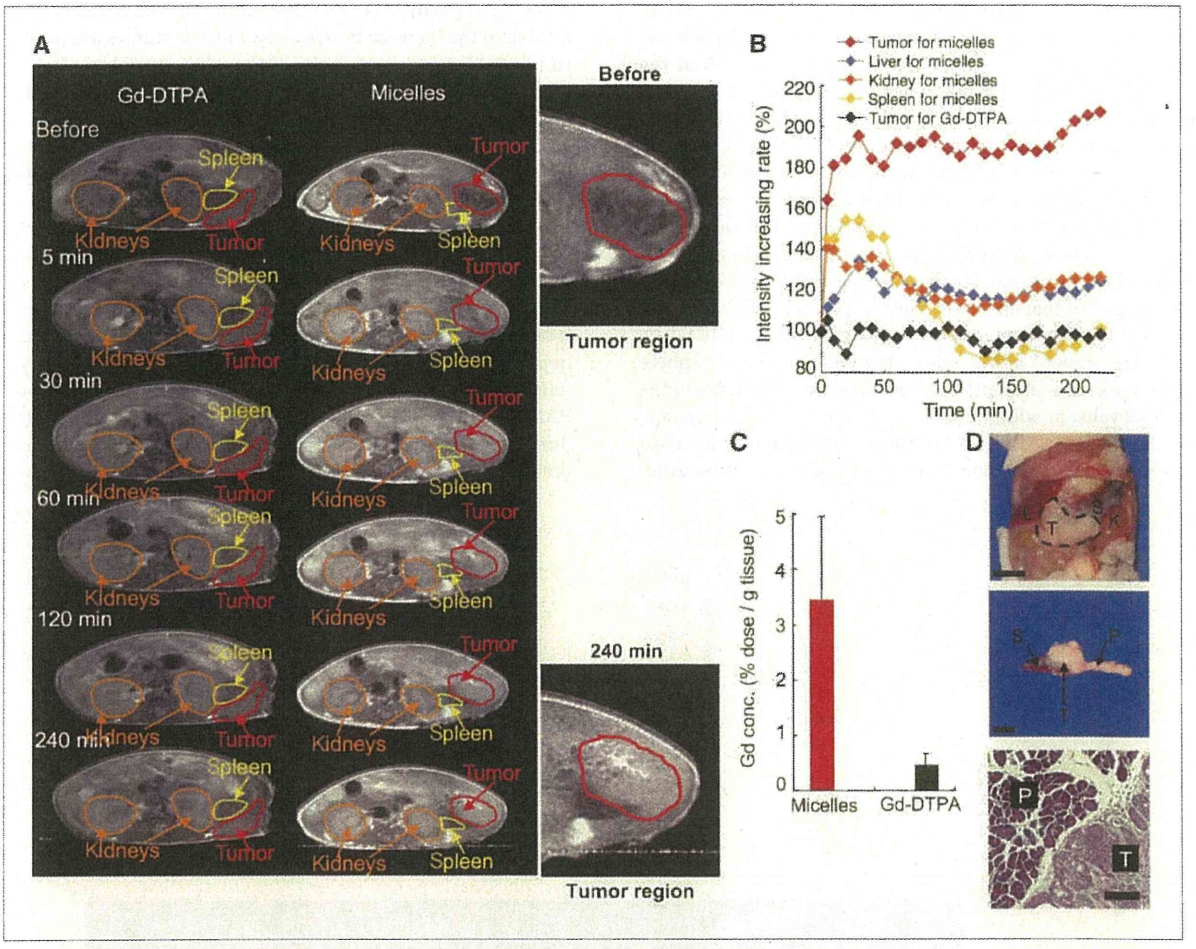

Figure 4. *In vivo* behavior of Gd-DTPA/DACHPt–loaded micelles on an orthotopic pancreatic cancer (BxPC3). A, *in vivo* MRI series of T_1-weighted transaxial slices of mice after i.v. injection of Gd-DTPA/DACHPt–loaded micelles or Gd-DTPA at 5 μmol/kg. B, relative MRI intensity in each organ after i.v. injection of Gd-DTPA/DACHPt–loaded micelles at 5 μmol/kg Gd-DTPA or i.v. injection of Gd-DTPA at 5 μmol/kg. C, the Gd-DTPA/DACHPt–loaded micelles and Gd-DTPA accumulation in the BxPC3 tumor 4 h after i.v. administration (n = 4). D, top, macroscopic findings of orthotopic BxPC3-bearing BALB/c nude mice after MRI acquisition. Scale bar, 1 cm. Pancreatic cancer (T), liver (L), kidney (K), and spleen (S). Middle, the pancreatic tumor after excision with spleen and normal pancreas. Scale bar, 0.5 cm. Bottom, microscopic findings (H&E staining) of the pancreatic cancer (T) and normal pancreatic tissue (P). Scale bar, 100 μm.

DACHPt–loaded micelles to assess the distribution of the anticancer drug at the tumor site by MRI.

Discussion

Pancreatic cancer has one of the worst prognoses among cancers (32). The high malignancy of pancreatic adenocarcinoma prompts the destruction of the surrounding tissue, whereas the lack of serous membrane in healthy pancreas cannot prevent the dissemination of cancer cells. The microenvironment characteristics of the pancreatic adenocarcinoma, including hypovascularity and thick fibrosis, prevent the accumulation of drugs in the tumor tissue (33). Moreover, the anatomic position of the pancreas in the deep retroperitoneal space makes early detection difficult. Although computed tomography is widely used for the evaluation of pancreatic carcinoma in the clinical setting, MRI may better predict the therapeutic efficacy and the prognosis in patients with pancreatic cancer because of its superior contrast resolution of noncontour deforming lesions of the pancreas, small liver metastases, and peritoneal disseminations (34). Thus, the outstanding contrast enhancement achieved by Gd-DTPA/DACHPt–loaded micelles on this tumor model suggests the great potential of this modality for the clear detection of the lesions in the abdominal cavity and the facile recognition of the carcinomas of the pancreas as distinct from the surrounding internal organs by MRI.

The exceptionally bright contrast achieved by Gd-DTPA/DACHPt–loaded micelles can be attributed to the enhanced accumulation of the micelles at the tumor site and to the

augmentation of the relaxivity of the Gd-DTPA in the core of the micelles. The amount of Gd-DTPA delivered by the micelles in the orthotopic pancreatic tumor was >3% of the injected dose after 4 hours. Because the r_1 of Gd-DTPA in the micelles is 24 times higher than that of free Gd-DTPA, the resulting contrast enhancement probably mimics a much higher accumulation level. In this regard, it has been reported that the r_1 of Gd-based MRI contrast agents increases after binding with polymers or proteins due to the flexibility reduction per Gd molecule and the increase of the rotational correlation time (τ_R; ref. 35). Moreover, Livramento and colleagues (36) suggested that an Fe/Gd chelate, a metallostar $Fe\{Gd_2(bipyridine(diethylenetriaminetetraacetic\ acid)_2(H_2O)_4)_3\}^{4-}$ structure, showed a high relaxivity because the inner-sphere water molecules presented an exchange rate (τ_m) close to the optimal value in addition to the increasing τ_R. In our system, the formation of the Gd-DTPA/DACHPt–loaded micelles probably combined an increase of the τ_R and the optimization of the τ_m in the hydrophobic environment at the micelle core, leading to the increase in relaxivity. Further studies are needed to establish the mechanism of the relaxivity enhancement of Gd-DTPA/DACHPt–loaded micelles, and they are currently under way in our laboratory.

The construction of macromolecular MRI contrast agents has been an attractive strategy to achieve diagnostic agents with extended blood circulation. Nevertheless, for Gd-based contrast agents, this approach could increase the risk of toxicity due to the prolonged tissue exposure to those macromolecules and the potential release of Gd^{3+} ions. Thus, the accumulation of high-generation dendrimer contrast agents in the healthy tissues might potentiate the nephrotoxicity and hepatotoxicity risks (37). Accordingly, only 20% of the injected dose of a generation 4–based PAMAM-Gd contrast agent was excreted from the body during the first 2 days, showing transient accumulation in the renal tubules. In contrast to this, the biodistribution of

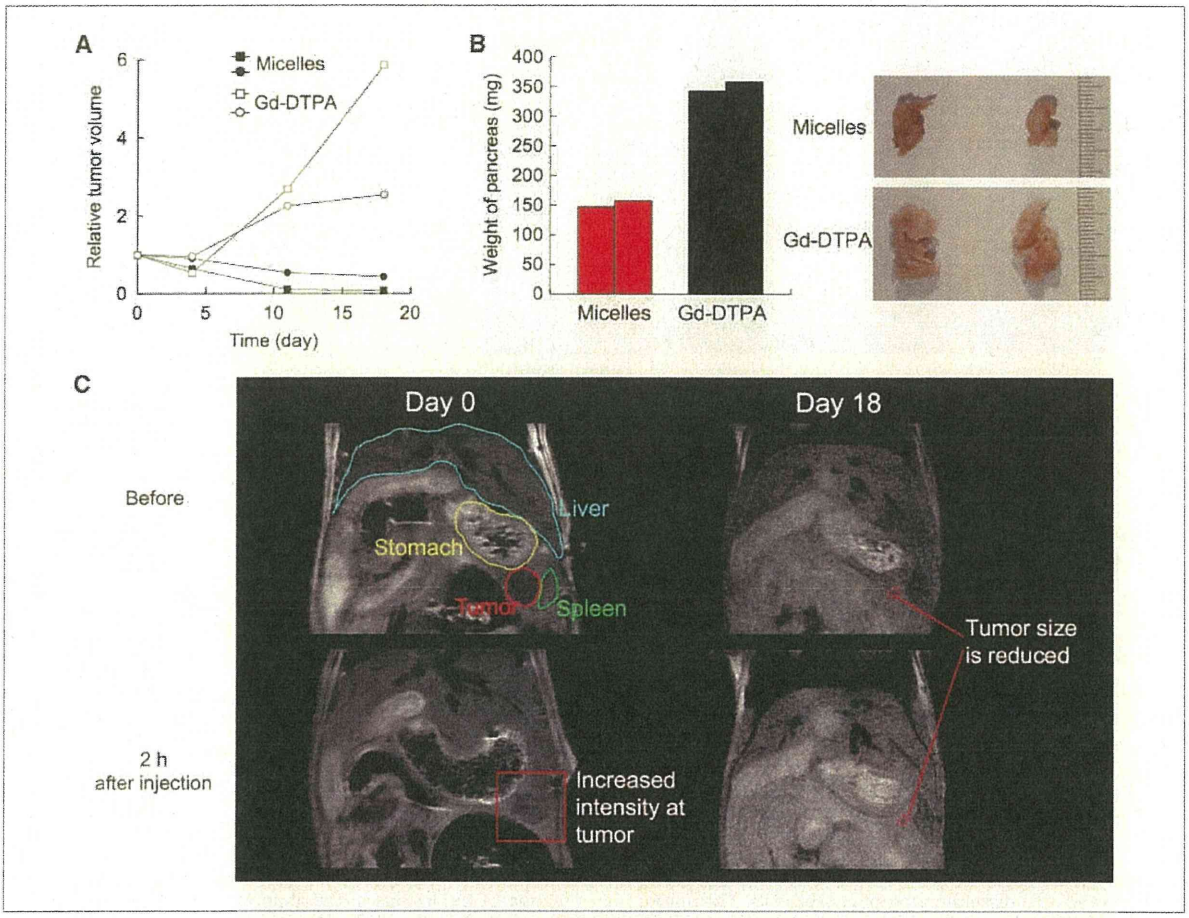

Figure 5. *In vivo* antitumor activity of Gd-DTPA/DACHPt–loaded micelles on orthotopic pancreatic cancer model (BxPC3) assessed by volumetric MRI. A, effect of Gd-DTPA/DACHPt–loaded micelles (8 mg/kg on Pt basis) and Gd-DTPA (30 mg/kg) injected i.v. at day 0, 4, 11 and 18 on the growth of BxPC3 tumors. B, left, weight of the whole pancreas for mice treated with the micelles or Gd-DTPA at day 18 on the antitumor experiment; right, macroscopies of the excised pancreas after treatment with the micelles or Gd-DTPA. C, MRI at days 0 and 18 of a tumor-bearing mouse treated with Gd-DTPA/DACHPt–loaded micelles. The tumor size was 89 mm^3 at day 0 and 5 mm^3 at day 18.

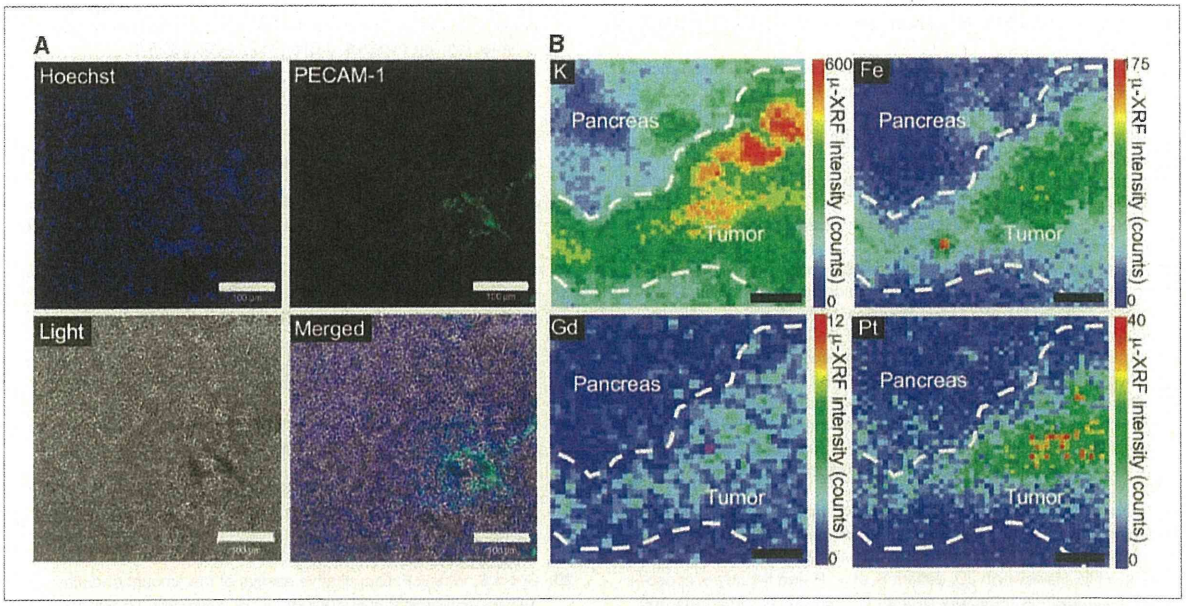

Figure 6. Intratumoral distribution of Gd-DTPA/DACHPt–loaded micelles in orthotopic BxPC3 tumors. A, immunofluorescence microscopy of tumor sections 4 h after injection of the micelles. The cell nuclei were stained with Hoechst, and the blood vessels were marked with PECAM-1 antibody. Scale bars, 100 μm. B, K, Fe, Pt, and Gd distribution in a tumor section including normal pancreatic tissue determined by μ-SR-XRF. Scale bars, 100 μm.

Gd-DTPA/DACHPt–loaded micelles revealed minimal accumulation of Gd-DTPA in normal tissues. Moreover, the Gd-DTPA released from the micelles probably is rapidly excreted from the body because of the relatively fast plasma clearance of low–molecular weight Gd-DTPA, thus eliminating the risk of undesired toxicity.

The real-time observation of drug distribution can increase the accuracy of treatment and enable practitioners to obtain feedback on the therapeutic efficacy at an earlier stage, and promptly adjust the treatment strategy. Gd-DTPA/DACHPt–loaded micelles might be helpful for directly assessing the distribution of the anticancer drugs at early stages by MRI. In this study, the μ-XRF results showed that the delivered Gd-DTPA and DACHPt were colocalized and uniformly distributed within the pancreatic tumors, whereas there was no drug accumulation in healthy pancreas, supporting the strong diagnostic and anticancer effect of the micelles (Fig. 6B, Pt and Gd). Moreover, the chemotherapy regimens are given in periodic cycles, for example, one cycle every 2 weeks during 12 weeks in FOLFOX (folinic acid, fluorouracil, and oxaliplatin) regimen for the treatment of colorectal cancer. By using Gd-DTPA/DACHPt–loaded micelles, the tumor size can be followed up in real-time by imaging at the day of the drug administration. Consequently, the Gd-DTPA/DACHPt–loaded micelles will have significant implications in the design and development of advanced multifunctional nanomedicines with great potential for clinical application as visible DDS.

Disclosure of Potential Conflicts of Interest

No potential conflicts of interest were disclosed.

Acknowledgments

We thank Sayaka Shibata and Teppei Nakahara for their technical assistance on the MRI experiments.

Grant Support

This research was supported by Funding Program for World-Leading Innovative R&D on Science and Technology (FIRST Program) from the Japan Society for the Promotion of Science (JSPS) and Grants-in-Aid for Scientific Research from the Japanese Ministry of Health, Labor, and Welfare (Nanomedicine Project).

The costs of publication of this article were defrayed in part by the payment of page charges. This article must therefore be hereby marked *advertisement* in accordance with 18 U.S.C. Section 1734 solely to indicate this fact.

Received 01/26/2010; revised 06/30/2010; accepted 07/09/2010; published OnlineFirst 08/04/2010.

References

1. Inoue A, Saijo Y, Maemondo M, et al. Severe acute interstitial pneumonia and gefitinib. Lancet 2003;361:137–9.
2. Jones BL. Trastuzumab: hopes and realities. Lancet Oncol 2002;3:137–44.
3. Ewer MS, Vooletich MT, Durand JB, et al. Reversibility of trastuzumab-related cardiotoxicity: new insights based on clinical course and response to medical treatment. J Clin Oncol 2005;23:7820–6.
4. Scappaticci FA, Skillings JR, Holden SN, et al. Arterial thromboembolic events in patients with metastatic carcinoma treated with chemotherapy and bevacizumab. J Natl Cancer Inst 2007;99:1232–9.

5. Davis ME, Chen Z, Shin DM. Nanoparticle therapeutics: an emerging treatment modality for cancer. Nat Rev Drug Discov 2008;7:771–82.
6. Torchilin VP. Recent advances with liposomes as pharmaceutical carriers. Nat Rev Drug Discov 2005;4:145–60.
7. Peer D, Karp JM, Hong S, Farokhzad OC, Margalit R, Langer R. Nanocarriers as an emerging platform for cancer therapy. Nature Nanotech 2007;2:751–60.
8. Ferrari M. Cancer nanotechnology: opportunities and challenges. Nat Rev Cancer 2005;5:161–71.
9. Duncan R. Polymer conjugates as anticancer nanomedicines. Nat Rev Cancer 2006;6:688–701.
10. Kabanov AV, Alakhov VY. Pluronic block copolymers in drug delivery: from micellar nanocontainers to biological response modifiers. Crit Rev Ther Drug Carrier Syst 2002;19:1–73.
11. Nishiyama N, Kataoka K. Current state, achievements, and future prospects of polymeric micelles as nanocarriers for drug and gene delivery. Pharmacol Ther 2006;112:630–48.
12. Matsumura Y, Kataoka K. Preclinical and clinical studies of anticancer agent-incorporating polymer micelles. Cancer Sci 2009;100:572–9.
13. Hashizume H, Baluk P, Morikawa S, et al. Opening between defective endothelial cells explain tumor vessel leakiness. Am J Pathol 2000;156:1363–80.
14. Maeda H. The enhanced permeability and retention (EPR) effect in tumor vasculature: the key role of tumor-selective macromolecular drug targeting. Adv Enzyme Regul 2001;41:189–207.
15. Muggia FM, Hainsworth JD, Jeffers S, et al. Phase II study of liposomal doxorubicin in refractory ovarian cancer: antitumor activity and toxicity modification by liposomal encapsulation. J Clin Oncol 1997;15:987–93.
16. Gradishar WJ, Tjulandin S, Davidson N, et al. Phase III trial of nanoparticle albumin-bound paclitaxel compared with polyethylated castor oil-based paclitaxel in women with breast cancer. J Clin Oncol 2005;23:7794–803.
17. Matsumura Y, Maeda H. A new concept for macromolecular therapeutics in cancer chemotherapy: mechanism of tumoritropic accumulation of proteins and the antitumor agent SMANCS. Cancer Res 1986;46:6387–92.
18. Hamaguchi T, Matsumura Y, Shirao K, et al. Phase I study of novel drug delivery system, NK911, a polymer micelle encapsulated doxorubicin [abstract 571]. Proceedings of the 39th annual meeting of the American Society of Clinical Oncology (ASCO); 2003, May 31-June 3; Chicago, USA.
19. Kato K, Hamaguchi T, Yasui H, et al. Phase I study of NK105, a paclitaxel-incorporating micellar nanoparticle, in patients with advanced cancer. ASCO Annual Meeting Proceedings. J Clin Oncol 2006;24:2018.
20. Burris HA III, Infante JR, Spigel DR, et al. A phase I dose-escalation study of NK012. ASCO Annual Meeting Proceedings. J Clin Oncol 2008;26:2538.
21. Wilson RH, Plummer R, Adam J, et al. Phase I and pharmacokinetic study of NC-6004, a new platinum entity of cisplatin-conjugated polymer forming micelles. J Clin Oncol 2008;26:2573.
22. Dent R, Trudeau M, Pritchard KI, et al. Triple-negative breast cancer: clinical features and patterns of recurrence. Clin Cancer Res 2007;13:4429–34.
23. McCarthy JR, Weissleder R. Multifunctional magnetic nanoparticles for targeted imaging and therapy. Adv Drug Deliv Rev 2008;60:1241–51.
24. McCarthy JR, Jaffer FA, Weissleder R. A macrophage-targeted theranostic nanoparticle for biomedical applications. Small 2006;2:983–7.
25. Pan D, Caruthers SD, Hu G, et al. Ligand-directed nanobialys as theranostic agent for drug delivery and manganese-based magnetic resonance imaging of vascular targets. J Am Chem Soc 2008;130:9186–7.
26. Nasongkla N, Bey E, Ren J, et al. Multifunctional polymeric micelles as cancer-targeted, MRI-ultrasensitive drug delivery systems. Nano Lett 2006;6:2427–30.
27. Weinmann HJ, Brasch RC, Press WR, Wesbey GE. Characteristics of gadolinium-DTPA complex: a potential NMR contrast agent. Am J Roentgenol 1984;142:619–24.
28. Cabral H, Nishiyama N, Okazaki S, Koyama H, Kataoka K. Preparation and biological properties of dichrolo(1,2-diaminocyclohexane) platinum(II) (DACHPt)-loaded polymeric micelles. J Control Release 2005;101:223–32.
29. Gouin S, Winnik F. Quantitative assays of the amount of diethylenetriaminepentaacetic acid conjugated to water-soluble polymers using isothermal titration calorimetry and colorimetry. Bioconjug Chem 2001;12:372–7.
30. Terada Y, Goto S, Takimoto N, et al. Construction and commissioning of BL37XU at SPring-8. AIP Conf Proc 2004;705:376–9.
31. Ventrucci M, Cipolla A, Racchini C, Casadei R, Simoni P, Gullo L. Tumor M2-pyruvate kinase, a new metabolic marker for pancreatic cancer. Dig Dis Sci 2004;49:1149–55.
32. Jemal A, et al. Cancer statistics, 2007. CA Cancer J Clin 2007;57:43–66.
33. Sofuni A, et al. Differential diagnosis of pancreatic tumors using ultrasound contrast imaging. J Gastroenterol 2005;40:518–25.
34. Miller FH, Rini NJ, Keppke AL. MRI of adenocarcinoma of the pancreas. Am J Roentgenol 2006;187:W365–374.
35. Zhang Z, Greenfield MT, Spiller M, McMurry TJ, Lauffer RB, Caravan P. Multilocus binding increases the relaxivity of protein-bound MRI contrast agents. Angew Chem 2005;117:6924–7.
36. Livramento JB, Toth E, Sour A, Borel A, Merbach AE, Ruloff R. High relaxivity confined to a small molecular space: a metallostar-based potential MRI contrast agent. Angew Chem Int Ed 2005;44:1480–4.
37. Duncan R, Izzo L. Dendrimer biocompatibility toxicity. Adv Drug Deliv Rev 2005;57:2215–37.

Direct and instantaneous observation of intravenously injected substances using intravital confocal micro-videography

Yu Matsumoto,[1,2,3] Takahiro Nomoto,[4] Horacio Cabral,[4] Yoko Matsumoto,[5] Sumiyo Watanabe,[1,6,7] R. James Christie,[8] Kanjiro Miyata,[1] Makoto Oba,[9] Tadayoshi Ogura,[10] Yuichi Yamasaki,[8] Nobuhiro Nishiyama,[1] Tatsuya Yamasoba,[2] and Kazunori Kataoka[1,4,8,*]

[1]Division of Clinical Biotechnology, Center for Disease Biology and Integrative Medicine, Graduate School of Medicine, The University of Tokyo, Japan
[2]Department of Otorhinolaryngology and Head and Neck Surgery, Graduate School of Medicine and Faculty of Medicine, The University of Tokyo, Japan
[3]Department of Otorhinolaryngology and Head and Neck Surgery, Mitsui Memorial Hospital, Japan
[4]Department of Bioengineering, Graduate School of Engineering, The University of Tokyo, Japan
[5]Department of Obstetrics and Gynecology, Graduate School of Medicine and Faculty of Medicine, The University of Tokyo, Japan
[6]Division of Nephrology and Endocrinology, Department of Internal Medicine, Graduate School of Medicine and Faculty of Medicine, The University of Tokyo, Japan
[7]Department of Internal Medicine, Teikyo University School of Medicine, Japan
[8]Department of Materials Engineering, Graduate School of Engineering, The University of Tokyo, Japan
[9]Department of Vascular Regeneration, Division of Tissue Engineering, The University of Tokyo Hospital, Japan
[10]Nikon Instech Co., Ltd., Japan
**kataoka@bmw.t.u-tokyo.ac.jp*

Abstract: We describe the development and application of intravital confocal micro-videography to visualize entrance, distribution, and clearance of drugs within various tissues and organs. We use a Nikon A1R confocal laser scanning microscope system attached to an upright ECLIPSE FN1. The Nikon A1R allows simultaneous four channel acquisition and speed of 30 frames per second while maintaining high resolution of 512 × 512 scanned points. The key techniques of our intravital imaging are (1) to present a flat and perpendicular surface to the objective lens, and (2) to expose the subject with little or no bleeding to facilitate optical access to multiple tissues and organs, and (3) to isolate the subject from the body movement without compressing the blood vessels, and (4) to insert a tail vein catheter for timed injection without moving the subject. Ear lobe dermis tissue was accessible without surgery. Liver, kidney, and subcutaneous tumor were accessed following exteriorization through skin incision. In order to image initial extravasations of compounds into tissue following intravenous injection, movie acquisition was initialized prior to drug administration. Our technique can serve as a powerful tool for investigating biological mechanisms and functions of intravenously injected drugs, with both spatial and temporal resolution.

OCIS codes: (170.1790) Confocal microscopy; (170.2655) Functional monitoring and imaging.

References and links

1. I. Veilleux, J. A. Spencer, D. P. Biss, D. Cote, and C. P. Lin, "In Vivo Cell Tracking With Video Rate Multimodality Laser Scanning Microscopy," IEEE J. Sel. Top. Quantum Electron. **14**(1), 10–18 (2008).
2. P. Kim, M. Puoris'haag, D. Côté, C. P. Lin, and S. H. Yun, "In vivo confocal and multiphoton microendoscopy," J. Biomed. Opt. **13**(1), 010501 (2008).
3. P. Kim, E. Chung, H. Yamashita, K. E. Hung, A. Mizoguchi, R. Kucherlapati, D. Fukumura, R. K. Jain, and S. H. Yun, "In vivo wide-area cellular imaging by side-view endomicroscopy," Nat. Methods **7**(4), 303–305 (2010).
4. R. Mehvar, M. A. Robinson, and J. M. Reynolds, "Molecular weight dependent tissue accumulation of dextrans: in vivo studies in rats," J. Pharm. Sci. **83**(10), 1495–1499 (1994).

#135496 - $15.00 USD Received 27 Sep 2010; revised 16 Oct 2010; accepted 17 Oct 2010; published 21 Oct 2010

5. R. Mehvar, and T. L. Shepard, "Molecular-weight-dependent pharmacokinetics of fluorescein-labeled dextrans in rats," J. Pharm. Sci. **81**(9), 908–912 (1992).
6. G. Zhang, V. Budker, and J. A. Wolff, "High levels of foreign gene expression in hepatocytes after tail vein injections of naked plasmid DNA," Hum. Gene Ther. **10**(10), 1735–1737 (1999).
7. F. Liu, Y. Song, and D. Liu, "Hydrodynamics-based transfection in animals by systemic administration of plasmid DNA," Gene Ther. **6**(7), 1258–1266 (1999).
8. H. Herweijer, and J. A. Wolff, "Progress and prospects: naked DNA gene transfer and therapy," Gene Ther. **10**(6), 453–458 (2003).
9. D. Liu, and J. E. Knapp, "Hydrodynamics-based gene delivery," Curr. Opin. Mol. Ther. **3**(2), 192–197 (2001).
10. A. Crespo, A. Peydró, F. Dasí, M. Benet, J. J. Calvete, F. Revert, and S. F. Aliño, "Hydrodynamic liver gene transfer mechanism involves transient sinusoidal blood stasis and massive hepatocyte endocytic vesicles," Gene Ther. **12**(11), 927–935 (2005).
11. T. Suda, X. Gao, D. B. Stolz, and D. Liu, "Structural impact of hydrodynamic injection on mouse liver," Gene Ther. **14**(2), 129–137 (2007).
12. G. Zhang, X. Gao, Y. K. Song, R. Vollmer, D. B. Stolz, J. Z. Gasiorowski, D. A. Dean, and D. Liu, "Hydroporation as the mechanism of hydrodynamic delivery," Gene Ther. **11**(8), 675–682 (2004).
13. Y. Ohno, H. Birn, and E. I. Christensen, "In vivo confocal laser scanning microscopy and micropuncture in intact rat," Nephron, Exp. Nephrol. **99**(1), e17–e25 (2005).

Introduction

In vivo imaging has received much attention in recent years, as it can elucidate the complex biological and pathological events within a living animal. Although histological examination of excised tissues has long served as a fundamental approach for tissue analysis, intravital confocal microscopy provides instant histopathology at the cellular and subcellular level and therefore is ideal for investigating dynamic events involved. Here we describe the development and application of intravital confocal micro-videography to visualize entrance, distribution, and clearance of drugs within various tissues and organs. In order to image initial extravasations of compounds into tissue following intravenous injection, movie acquisition was initialized prior to drug administration. Many groups have adapted commercial confocal microscopes for intravital imaging, but they often use conventional galvano scanners with slow acquisition speed. Progressive groups build confocal and/or multi-photon microscopes and even microendoscopes with rapid scanning systema in-house to achieve video-rate imaging [1–3].

Table 1. Commercially available rapid scanning confocal microscopes

Vendor	Product Name	Scanning System	Maximum Frame Rate at 512 x 512 Pixels	Number of Simultaneously Detectable Channels
Nikon	A1R	Resonant Scanner	30 fps	4
Leica Microsystems	TCS SP5 II	Resonant Scanner	25 fps	5
Carl Zeiss	LSM 7 LIVE	Linear Scanner	120 fps	2
Yokogawa Electric	CSU-X1	Nipkow spinning disk	2000 fps	3
Olympus	DSU	Spinning Disk Confocal	15 fps	1

Recently, several rapid scanning confocal microscopes became commercially available (Table 1). Although all vendors primarily recommend use of their products with an inverted configuration (optimized for live cell imaging), combination with an upright microscope has advantages for intravital imaging. Here, we attached a Nikon A1R confocal laser scanning microscope system to an upright ECLIPSE FN1 to acquire video images. The A1R incorporates both a conventional galvano scanner and also a high-speed resonant scanner, which allows an acquisition speed of 30 frames per second and simultaneous four channel detection, while maintaining high resolution of 512 × 512 scanned points.Our technique consists of the following essential features:

(1) Front-end design presenting a flat and perpendicular surface against the objective lens;

#135496 - $15.00 USD Received 27 Sep 2010; revised 16 Oct 2010; accepted 17 Oct 2010; published 21 Oct 2010

(2) Exposure surgery with little or no bleeding to facilitate optical access to multiple tissues and organs;

(3) Stabilization of the sample to isolate from the body movement without compressing the blood vessels;

(4) Tail vein catheterization for timed injection during data acquisition, without moving the subject;

Our technique is particularly effective for investigating the dynamic and complex events that occur immediately following drug administration. We investigated the influence of molecular weight on pharmacokinetic behavior by imaging the ear lobe dermis. We also investigated the accumulation of pDNA within liver tissue by hydrodynamic injection. Kidney and tumor tissues were imaged to observe renal excretion and tumor extravasation.

Results and discussion

During the development of a promising drug delivery system, there is a strong need to accurately grasp the intravital behavior of the administered drugs [4,5]. We investigated the influence of molecular weight on pharmacokinetic behavior using fluorescein (MW = 332) and fluorescein-labeled dextrans (FD) with average molecular weights of 10-, 40-, and 500 kDa (Fig. 1). Fluorescein and FDs demonstrated different pharmacokinetics [Fig. 1(c), 1(e), Media 1, Media 2, Media 3, and Media 4]. Arterial entrance was observed 10 seconds after injection, followed by venous migration 30 seconds after injection. Fluorescein diffused into extravascular tissue concurrently with venous migration. FD 10 kDa gradually translocated into extravasculature tissue 10-15 minutes after injection and lymphatic drainage was observed after 20 minutes. FD 70- and 500 kDa remained in the vasculature during the entire 60-minute observation period. Our confocal micro-videography technique is superior to conventional methods used to study plasma clearance in regard to the number of animals needed to generate a clearance curve and also the ability to obtain more information from a single experiment. Conventional protocols used in plasma clearance studies require blood extraction at various post-injection time points, using multiple animals. In contrast, intravital confocal micro-videography yields 30 time points per seconds before, during, and after the injection. Moreover, our technique provides spatial resolution so that we can individually investigate multiple regions such as arteries, veins, extravascular tissue, lymphatic vessels, and even cells and nuclei if desirable [Fig. 1(d)]. For long-term plasma clearance studies, however, we still perform conventional methods in conjunction with our technique because prolonged anesthesia periods longer than five hours are not practical.

#135496 - $15.00 USD Received 27 Sep 2010; revised 16 Oct 2010; accepted 17 Oct 2010; published 21 Oct 2010

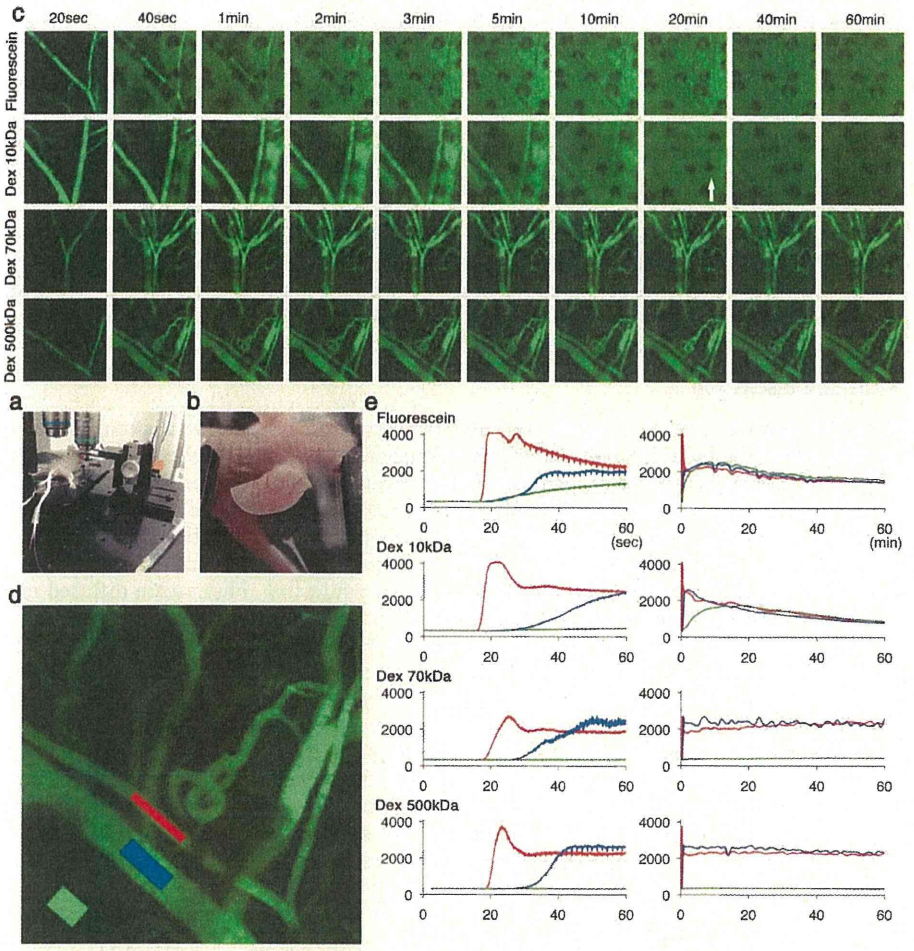

Fig. 1. (a) The earlobe is an excellent location for intravital confocal micro-videography because blood vessels are easily observed in the dermis and the ear is easily accessed and positioned in the imaging apparatus. (b) Earlobe was attached to the coverslip with a small drop of immersion oil. (c) Fluorescein, FD 10-, 70-, and 500 kDa were administered via tail vein catheter 10 seconds after movie acquisition was initiated. Video-rate (30 fps) movies were recorded for the first minute, and subsequent time-lapse images were recorded every minute for an additional 60 minutes. The arrow indicates lymphatic drainage. Obtained data sets were further processed using Nikon NIS-Elements C software. Image size: 645.50μm x 645.50μm. (d) Three regions of interest (ROI) are selected respectively as an artery (red), vein (blue), and extravascular skin tissue (green). Image size: 645.50μm x 645.50μm. (e) Fluorescence intensity in these ROIs plotted against time. All movies are provided as supplementary movie files (Media 1, Media 2, Media 3, and Media 4).

The liver is a vital organ that has a wide range of functions, including detoxification, protein synthesis, storage, and production of bile. Real-time imaging of liver dynamics and small changes in hepatocytes will provide insight to poorly understood processes that occur in the liver. We applied our real-time imaging technique to observe the accumulation of pDNA within liver tissue by hydrodynamic injection [Fig. 2(a)]. Delivery of pDNA by hydrodynamic injection involves rapid tail vein injection of a large volume of pDNA solution and efficient accumulation of pDNA in the liver is reported [6,7]. This method has been widely utilized by the gene therapy community for evaluating therapeutic activities of various genes [8,9].

#135496 - $15.00 USD Received 27 Sep 2010; revised 16 Oct 2010; accepted 17 Oct 2010; published 21 Oct 2010

Following normal injection, pDNA flowed into the hepatic lobule from the hepatic artery, through the sinusoids, and towards the central vein (Media 5). After 20 minutes, pDNA was observed adjacent to vessel walls, but was rarely transferred into hepatic cells. In contrast, hydrodynamic injection of pDNA resulted in initial flow into the hepatic lobule from the hepatic artery, but the flow stopped at the sinusoids. After 50 seconds, pDNA appeared from the central vein, indicating retrodynamic blood flow. Blood flow oscillated back and forth within the sinusoids, indicating that the blood pressure of central and portal vein remained in equilibrium, which lasted as long as 3 minutes (Media 6). During the 30-minute period after injection, pDNA was observed in more hepatic cell nuclei by hydrodynamic injection than normal injection. It has been hypothesized that hydrodynamic injection generates retrodynamic blood flow from the central vein [10–12]. This hypothesis was well described by performing dual pressure detector system of the portal vein and inferior vena cava, and is further supported by our results obtained by direct imaging of the hepatic lobule.

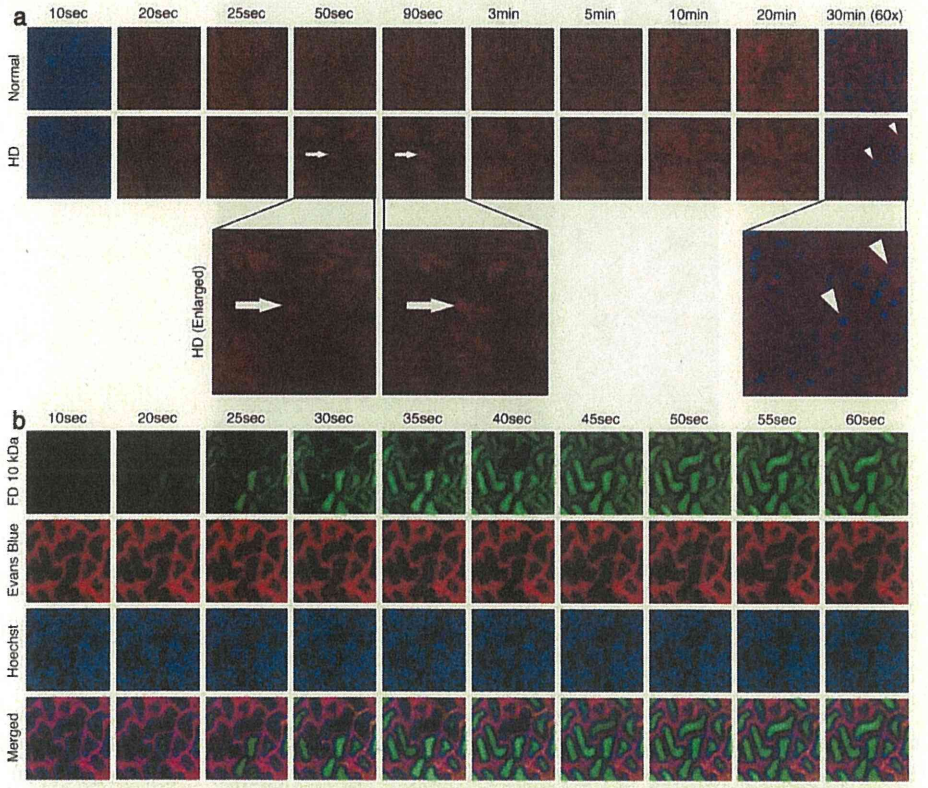

Fig. 2. (a) Intravital confocal micro-videography of the mouse hepatic lobule. Hoechst (blue) was intravenously injected 15 minutes before imaging. Cy5-labeled pDNA (red) were normally or hydrodynamically (HD) injected via tail vein catheter 10 seconds after movie acquisition was initiated (Media 5 and Media 6). Image frames were extracted from both videos at identical time points for comparison. Image size: 645.50μm x 645.50μm. Zoomed pictures were taken 30 minutes after injection. Image size: 212.13μm x 212.13μm. Hoechst channels are shown at 10 sec and 30 min for histological comprehension. Arrows indicate reverse blood flow from central vein. Arrowheads indicate nuclei that pDNA were successfully transferred. (b) Intravital confocal micro-videography of mouse kidney tissue. Hoechst (blue) and Evan's Blue dye (red) were intravenously injected 15 minutes and 5 minutes before imaging, respectively. FD 10 kDa (green) were administered via tail vein catheter 10 seconds after movie acquisition was initiated (Media 7). Image size: 645.50μm x 645.50μm.

#135496 - $15.00 USD Received 27 Sep 2010; revised 16 Oct 2010; accepted 17 Oct 2010; published 21 Oct 2010

To further demonstrate the feasibility of our technique, kidney and tumor tissues were imaged to observe renal excretion and tumor extravasation. Deeper kidney structures such as glomeruli could not be imaged because renal tissue highly absorbs and scatters light [13]. Although the imaging of the renal cortex was limited to shallow features such as proximal and distal tubules and capillary vessels, we still could evaluate glomerular filtration indirectly [Fig. 2(b)]. FD 10 kDa flowed into the capillary blood vessels and proximal tubules at the same time, which indicate that FD 10 kDa were immediately filtered by glomerulus. FD 10 kDa flowed into the distal tubules shortly afterward, until all the tubules were filled. The albumin - Evan's blue dye complex remained in blood circulation throughout the study for 60 minutes. Observation of the albumin - Evan's blue dye complex also depicted tumor vasculature [Fig. 3(a)]. Multiple frames were merged to produce a wide-area image [Fig. 3(b)].

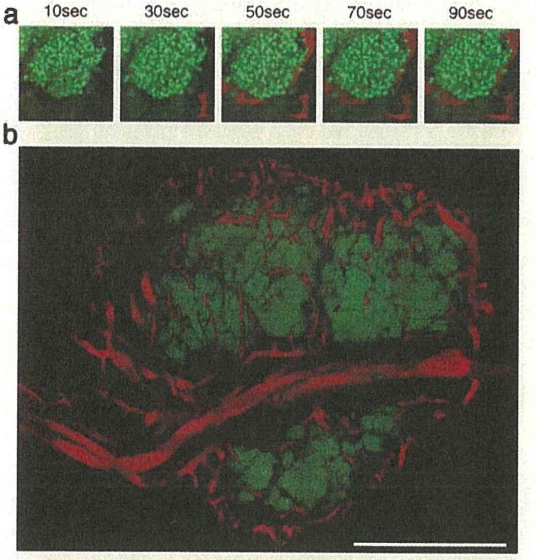

Fig. 3. (a) Intravital confocal micro-videography of subcutaneous HeLa-H2BGFP tumor. Evan's blue dye was administered via tail vein catheter 10 seconds after movie acquisition was initiated. Image frames were extracted from the video at indicated time points. Image size: 212.13μm x 212.13μm (b) Motorized XY stage enables 'large image acquisition' feature of the Nikon NIS-Elements C software. Multiple frames were automatically captured in sequence and merged to produce a wide-area image. Scale bar: 1 mm.

Arterial entrance, venous migration, extravasation into tissue, and clearance was directly observed within various tissues and organs. The intravital confocal micro-videography technique described here is useful for investigating biological mechanisms and functions in both spatial and temporal resolution. Our technique is particularly effective for investigating the dynamic and complex events that occur immediately following drug administration, such as first path effects, site-specific drug accumulation, blood circulation and metabolism behavior.

Materials and methods

Microscope

All picture/movie acquisitions were performed using a Nikon A1R confocal laser scanning microscope system attached to an upright ECLIPSE FN1 (Nikon Corp., Tokyo, Japan). The A1R incorporates both conventional a galvano scanner and also a high-speed resonant scanner. The resonant scanner allows an acquisition speed of 30 frames per second while

#135496 - $15.00 USD Received 27 Sep 2010; revised 16 Oct 2010; accepted 17 Oct 2010; published 21 Oct 2010